DISSERTATION

TRANSIENT ANALYSIS OF CLOSED- AND OPEN-REGION ELECTROMAGNETIC PROBLEMS USING HIGHER ORDER FINITE ELEMENT METHOD AND METHOD OF MOMENTS IN THE TIME DOMAIN

Submitted by

Nada J. Šekeljić

Department of Electrical and Computer Engineering

In partial fulfillment of the requirements

For the Degree of Doctor of Philosophy

Colorado State University

Fort Collins, Colorado

Spring 2015

Doctoral Committee:

Advisor: Branislav M. Notaroš

Jennifer Mueller
Steven C. Reising
V. Chandrasekar
Milan M. Ilić

ABSTRACT

TRANSIENT ANALYSIS OF CLOSED- AND OPEN-REGION ELECTROMAGNETIC PROBLEMS USING HIGHER ORDER FINITE ELEMENT METHOD AND METHOD OF MOMENTS IN THE TIME DOMAIN

The principal objective of this dissertation is to develop computational electromagnetic (CEM) methodology and tools for modeling of closed (waveguide and cavity based) and open (radiation and scattering) electromagnetic structures in the time domain (TD), employing two CEM approaches. The first method is a novel higher order and large-domain Galerkin finite element method (FEM) for transient analysis of multiport microwave waveguide devices with arbitrary metallic and dielectric discontinuities. It is based on geometrical modeling using Lagrange interpolation generalized hexahedral elements, spatial field expansion in terms of hierarchical curl-conforming polynomial vector basis functions, time-stepping with an implicit unconditionally stable finite difference scheme using the Newmark-beta method, and mesh truncation introducing the waveguide port boundary condition. The second method is a novel spatially large-domain and temporally entire-domain method of moments (MoM) proposed for surface integral equation (SIE) modeling of 3-D conducting scatterers in the TD. The method uses higher order curved Lagrange interpolation generalized quadrilateral geometrical elements, higher order spatial current expansions based on hierarchical divergence-conforming polynomial vector basis functions, and temporal current modeling by means of orthogonal weighted associated Laguerre basis functions. It implements full temporal and spatial Galerkin testing and marching-on-in-degree (MOD) scheme for an iterative solution of the final system of spatially

and temporally discretized MoM-TD equations. Numerical examples of waveguides and scatterers, modeled using flat and curved large elements in conjunction with field/current expansions of orders from 2 to 9, demonstrate excellent accuracy, efficiency, convergence, and versatility of the proposed methodologies. The results obtained by higher order TD-FEM and TD-MoM are in an excellent agreement with indirect solutions obtained from FEM and MoM analyses in the frequency domain (FD) in conjunction with discrete Fourier transform and its inverse, as well as with measurements and alternative full-wave numerical solutions in both TD and FD.

ACKNOWLEDGEMENTS

I would like to express my sincere gratitude to my advisor, Professor Branislav Notaroš, for his valuable support and guidance during my graduate studies at Colorado State University. The work in this dissertation has been benefited from his many years of research and teaching experience.

I especially thank Professor Milan Ilić who inspired my research interest in numerical methods and computational electromagnetics. Also, I appreciate all of the scientific conversations we have had since my undergraduate studies at School of Electrical Engineering (ETF), University of Belgrade.

I am grateful to all former and present students of the EMAG Lab for their friendship and their support during these years at CSU.

All my accomplishments would not have been possible without my adorable family who always believed in me. Finally, I thank my husband Julio Cesar for his priceless help, encouragement, and optimism in this journey.

TABLE OF CONTENTS

1 HIGHER ORDER FINITE ELEMENT METHOD FOR VECTOR WAVE EQUATION MODELING IN TIME DOMAIN[1]

1.1 Introduction

The finite element method (FEM) has been effectively used in full-wave three-dimensional (3-D) solutions to both open-region (e.g., antenna and scattering) and closed-region (e.g., waveguide and cavity) problems based on discretizing partial differential equations (PDEs) in electromagnetics [1]–[6]. The FEM has been well established as a method of choice for analysis and design of waveguide-based multiport passive microwave devices and systems, of arbitrary shapes and material compositions, in the frequency domain (FD) [7]–[11]. A rather disproportionate body of work exists, on the other hand, in the development of methods and tools for the FEM analysis and modeling in the time domain (TD) [1], [2], [6], [12]–[24], in spite of the fact that TD analysis and characterization of microwave structures and evaluation of associated transient electromagnetic phenomena are also of great practical importance for a number of well-established and emerging areas of microwave theory and engineering.

FEM techniques for direct modeling of electromagnetic phenomena in the time domain (TDFEM techniques) are based on a direct numerical discretization of TD PDEs governing such phenomena (Maxwell's equations or wave equations in the time domain) [1], [2], [6], [12]–[23]. Alternatively, the TD response of a microwave structure can be obtained indirectly, using the FEM analysis in the frequency domain (FDFEM) in conjunction with the discrete Fourier transform (DFT) and its inverse (IDFT) [24]. Efficient FDFEM-DFT/IDFT modeling of

waveguide discontinuities and the first time-from-frequency-domain FEM solver are presented in [24]. This present paper focuses on the TDFEM (direct) approach.

In terms of the particulars of the numerical discretization in space, practically all the existing 3-D TDFEM electromagnetic tools are low-order (also referred to as small-domain or sub-domain) techniques, with the electromagnetic structure being modeled by volume geometrical elements (most frequently, tetrahedra with planar sides) that are electrically very small and the fields within the elements are approximated by low-order (zeroth-order and first-order) basis. This results in a very large number of unknowns (unknown field-distribution coefficients) needed to obtain results of satisfactory accuracy, with all the associated problems and large requirements in computational resources. An alternative approach, the higher order (also known as the large-domain or entire-domain) computational approach, which utilizes higher order basis functions defined in large curved geometrical elements, and which can greatly reduce the number of unknowns for a given problem and enhance the accuracy and efficiency of the computation [25], seems to have not been fully employed in the TDFEM analysis yet. Namely, almost none of the reported TDFEM results and applications in the literature demonstrate actual using and implementation of models of orders higher than two (high-order modeling). Notable examples of high-order TDFEM modeling are the transfinite-element TD method for analysis of multiport waveguide structures proposed in [20], where nearly orthogonal Nedelec hierarchical bases of orders from zero to three are used, and TDFEM solutions to cavity and waveguide problems in [23], where the results for hierarchical basis functions of up to mixed fourth order (order 3.5) on tetrahedral cells are presented. In addition, none of the works employ large elements (or a combination of large and small elements) in the TDFEM model (large-domain modeling).

This dissertation proposes a novel higher order and large-domain Galerkin-type finite element method for 3-D electromagnetic modeling in the time domain based on higher order geometrical modeling, higher order field modeling, and an implicit unconditionally stable time-stepping finite difference scheme invoking the Newmark-beta method, and presents its implementation in the TDFEM analysis of multiport microwave waveguide devices with arbitrary metallic and dielectric discontinuities. The geometry of the structure is modeled using Lagrange-type interpolation generalized hexahedra of arbitrary geometrical-mapping orders, and the fields in the elements are expanded in terms of hierarchical curl-conforming 3-D polynomial vector basis functions of arbitrarily high field-approximation orders. The finite element mesh is truncated introducing the waveguide port boundary condition (WPBC) at the waveguide ports, which is able to launch an incident wave into the waveguide and at the same time absorb the reflections from waveguide discontinuities in the 3-D TDFEM analysis [21]. Once the TD solution is obtained, the broadband frequency response (if needed) is computed applying the DFT to the TDFEM solution in the postprocessing.

Proposed technique represents the first truly higher order 3-D TDFEM method (the results demonstrate using field expansions of orders from 2 to 9) and the first set of large-domain TDFEM modeling examples (the examples demonstrate very effective large-domain TDFEM models of 3-D waveguide discontinuities using minimal numbers of large conformal finite elements and minimal numbers of unknowns). Overall, the examples demonstrate excellent accuracy, efficiency, stability, convergence, and versatility of the presented method.

1.2 Finite-Element Spatial Discretization

Consider a general multiport waveguide structure with an arbitrary metallic and/or dielectric discontinuity shown in Fig.1.1. In order to apply the FEM analysis, the computational domain is first truncated by imposing fictitious planar surfaces at each of the ports.

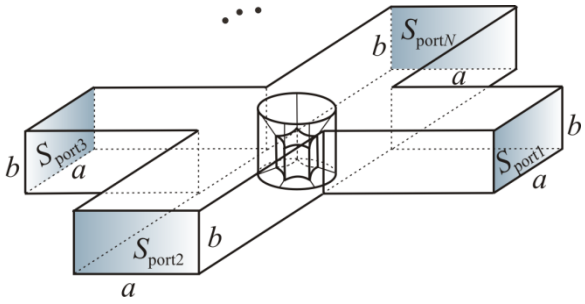

Figure 1.1. 3-D multiport waveguide structure with an arbitrary discontinuity, simulated by a higher order TDFEM method.

The bounded structure thus obtained is then tessellated using Lagrange-type generalized parametric hexahedra of arbitrary geometrical orders K_u, K_v, and K_w (K_u, K_v, $K_w \geq 1$), analytically described as [4]

$$\mathbf{r}(u,v,w) = \sum_{m=0}^{K_u}\sum_{n=0}^{K_v}\sum_{p=0}^{K_w}\mathbf{r}_{mnp}\, L_m^{K_u}(u)\, L_n^{K_v}(v)\, L_p^{K_w}(w), \qquad -1 \leq u,v,w \leq -1, \tag{1.1}$$

with $\mathbf{r}_{mnp} = \mathbf{r}(u_m, v_n, w_p)$ being the position vectors of interpolation nodes and $L_m^{K_u}$ representing Lagrange interpolation polynomials

$$L_m^{K_u}(u) = \prod_{l=0, l\neq m}^{K_u} \frac{u-u_l}{u_m-u_l}, \tag{1.2}$$

and similarly for $L_n^{K_v}(v)$ and $L_p^{Kw}(w)$. Equations (1.1) and (1.2) define a mapping from a cubical parent domain to a generalized hexahedron, as shown in Fig. 1.2.

The same Lagrange interpolating scheme is used to model continuously inhomogeneous material properties of a hexahedron (if applicable) in the mesh [11].

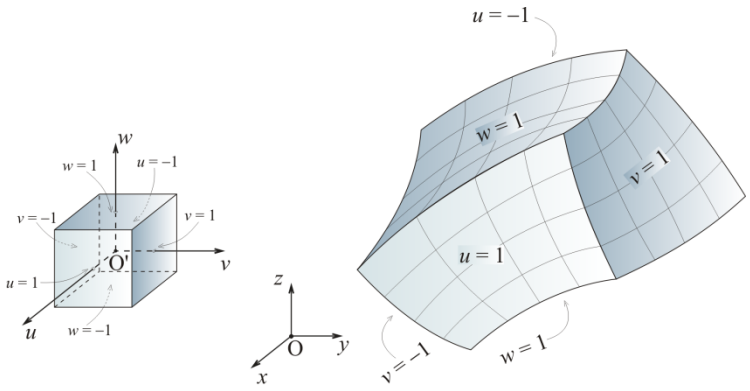

Figure 1.2. Generalized curved parametric hexahedron defined by (1.1) and (1.2); cubical parent domain is also shown.

1.3 Time Domain Finite Element Method Formulation

The general waveguide problem in Fig. 1.1 can be analyzed in the time domain starting from the source-free time-dependent Maxwell's equations. Considering a linear, homogeneous or continuously inhomogeneous medium within a finite-sized computational domain *V*, bounded by the surface *S*, the following time-dependent electric field vector wave equation is obtained, which, together with associated initial and boundary conditions, defines a well-known boundary value problem [1], [6]:

$$\nabla \times \frac{1}{\mu_r} \nabla \times \mathbf{E}(\mathbf{r},t) + \frac{1}{c_0^2} \varepsilon_r \frac{\partial^2 \mathbf{E}(\mathbf{r},t)}{\partial t^2} = 0 \tag{1.3}$$

where ε_r and μ_r are relative permittivity and permeability of the medium, respectively, and c_0 is the speed of light ($c_0 = 1/\sqrt{\varepsilon_0 \mu_0}$). By multiplying (1.3) with space-dependant weighted (testing) vector functions (independent of time), $\mathbf{w}(\mathbf{r})$, integrating over the domain *V* (weighted residual

method), and applying the first Green's vector identity, the weak formulation of the vector wave equation in the time domain is derived as follows:

$$\int_V \frac{1}{\mu_r}(\nabla\times\mathbf{w}(\mathbf{r}))\cdot(\nabla\times\mathbf{E}(\mathbf{r},t))\mathrm{d}V+\oint_S \frac{1}{\mu_r}(\mathbf{n}\times\nabla\times\mathbf{E}(\mathbf{r},t))\cdot\mathbf{w}(\mathbf{r})\mathrm{d}S+\frac{1}{c_0^2}\int_V \varepsilon_r\mathbf{w}(\mathbf{r})\cdot\frac{\partial^2\mathbf{E}(\mathbf{r},t)}{\partial t^2}\mathrm{d}V=0 \tag{1.4}$$

with $\mathbf{n}$ standing for the outward-looking unit normal to the surface *S*. Within each finite element in Fig. 1.2, the time-variant electric field intensity vector is expanded using higher order hierarchical-type curl-conforming vector basis functions $\mathbf{f}$ and unknown time-dependent coefficients $\alpha(t)$

$$\mathbf{E}(\mathbf{r},t)=\sum_{i=0}^{N_u-1}\sum_{j=0}^{N_v}\sum_{k=0}^{N_w}\alpha_{uijk}(t)\mathbf{f}_{uijk}+\sum_{i=0}^{N_u}\sum_{j=0}^{N_v-1}\sum_{k=0}^{N_w}\alpha_{vijk}(t)\mathbf{f}_{vijk}+\sum_{i=0}^{N_u}\sum_{j=0}^{N_v}\sum_{k=0}^{N_w-1}\alpha_{wijk}(t)\mathbf{f}_{wijk} \tag{1.5}$$

where the functions $\mathbf{f}$ are defined as [4]

$$\mathbf{f}_{uijk}=u^i P_j(v)P_k(w)\mathbf{a}'_u,\qquad \mathbf{f}_{vijk}=P_i(u)v^j P_k(w)\mathbf{a}'_v,\qquad \mathbf{f}_{wijk}=P_i(u)P_j(v)w^k\mathbf{a}'_w. \tag{1.6}$$

The *P*-functions are simple polynomials representing a higher-order generalization of one-dimensional rooftop functions

$$P_i(u)=\begin{cases}1-u, & i=0\\ u+1, & i=1\\ u^i-1, & i\geq 2,\text{ even}\\ u^i-u, & i\geq 3,\text{ odd}\end{cases},\quad -1\leq u,v,w\leq 1. \tag{1.7}$$

Parameters N_u, N_v, and N_w ($N_u, N_v, N_w \geq 1$) are the adopted orders of the polynomials along *u*-, *v*-, and *w*-directions of the local parametric coordinate system of each hexahedral element. Hierarchical functions $\mathbf{f}$ enable using different approximation orders in different elements in the model for efficient selective discretization of the solution domain, because each lower-order set of functions is a subset of higher-order sets. The reciprocal unitary vectors $\mathbf{a}'_u$, $\mathbf{a}'_v$, and $\mathbf{a}'_w$ in (1.6) are obtained as $\mathbf{a}'_u=(\mathbf{a}_v\times\mathbf{a}_w)/J$, $\mathbf{a}'_v=(\mathbf{a}_w\times\mathbf{a}_u)/J$, and $\mathbf{a}'_w=(\mathbf{a}_u\times\mathbf{a}_v)/J$, with $J=(\mathbf{a}_u\times\mathbf{a}_v)\cdot\mathbf{a}_w$ being the Jacobian of the covariant transformation and $\mathbf{a}_u=\partial\mathbf{r}/\partial u$, $\mathbf{a}_v=\partial\mathbf{r}/\partial v$,

and $\mathbf{a}_w = \partial\mathbf{r}/\partial w$ the unitary vectors, where $\mathbf{r}$ is given in (1.1). Substituting (1.5) into (1.3) and applying the Galerkin testing procedure (testing functions are the same as basis functions), the following semi-discrete system of linear equations, expressed in the matrix form, is obtained:

$$[A]\{\alpha(t)\} + \frac{1}{c_0^2}[B]\frac{\mathrm{d}^2\{\alpha(t)\}}{\mathrm{d}t^2} = G \tag{1.8}$$

where the column vector of unknown coefficients is given by $\{\alpha(t)\} = \{\{\alpha_u(t)\}, \{\alpha_v(t)\}, \{\alpha_w(t)\}\}^{\mathrm{T}}$, and the entries of matrices $[A]$ and $[B]$ are calculated as

$$A_{i,j} = \int_V \frac{1}{\mu_r}(\nabla\times\mathbf{f}_i)\cdot(\nabla\times\mathbf{f}_j)\mathrm{d}V \qquad B_{i,j} = \int_V \varepsilon_r\mathbf{f}_i\cdot\mathbf{f}_j\,\mathrm{d}V, \quad i=1,2,...N, \quad j=1,2,...N \tag{1.9}$$

where $\mathbf{f}_i$ and $\mathbf{f}_j$ symbolically represent testing and basis functions defined in (1.6) and (1.7), and N is the total number of basis/testing functions. Note that matrices $[A]$ and $[B]$ are completely time-independent and are computed only once. The right-hand side of (1.8) is intentionally left in the form

$$G = -\oint_S \frac{1}{\mu_r}\mathbf{f}_i\cdot(\mathbf{n}\times(\nabla\times\mathbf{E}(\mathbf{r},t)))\mathrm{d}S \tag{1.10}$$

as this surface integral conveniently provides the interface for excitation and reflectionless truncation of the finite element mesh, which is explained in the following sections.

1.4 Waveguide Port Boundary Condition in the Frequency Domain

Due to the continuity of the tangential component of the magnetic field intensity vector, $\mathbf{n}\times\mathbf{H}$, and hence the vector $\mathbf{n}\times(\nabla\times\mathbf{E})$ in (1.10) across the interface between any two finite elements in the FEM model, the right-hand side in (1.8) contains the surface integral (1.10) across the overall boundary of the entire FEM domain, and not over the internal boundary surfaces between the

individual finite elements in the model, which for the waveguide problem reduces to the surface integral across the waveguide ports. The total electric field vector at a cross section of a waveguide with discontinuities can be expressed as a superposition of the incident electric field and reflections from discontinuities that are modeled as a sum of orthogonal waveguide modes [1], [6],

$$\mathbf{E}(x,y,z)=\mathbf{E}^{\text{inc}}(x,y,z)+\sum_{m=0}^{\infty}\sum_{n=0}^{\infty}a_{mn}\mathbf{e}_{tmn}^{\text{TE}}(x,y)e^{\gamma_{mn}z}+\sum_{m=1}^{\infty}\sum_{n=1}^{\infty}b_{mn}[\mathbf{e}_{tmn}^{\text{TM}}(x,y)+\hat{z}\mathbf{e}_{zmn}^{\text{TM}}(x,y)]e^{\gamma_{mn}z} \tag{1.11}$$

where $\mathbf{e}_{tmn}^{\text{TE}}$ and $\mathbf{e}_{tmn}^{\text{TM}}$ are transversal components of eigen-functions for arbitrary TE and TM modes, respectively, and γ_{mn} is the propagation constant of the corresponding mode. If the waveguide operates in the dominant-mode regime and it is assumed that the ports are placed far enough from all discontinuities, substituting (1.11) into $\mathbf{n}\times(\nabla\times\mathbf{E})$ in (1.10) and taking advantage of the orthogonality property of eigen- functions, the following boundary condition at the ports can be derived:

$$\mathbf{n}\times(\nabla\times\mathbf{E})=\begin{cases}-2\gamma_{10}\mathbf{E}^{\text{inc}}+\gamma_{10}\mathbf{E} & \text{(excitation port)}\\ \gamma_{10}\mathbf{E} & \text{(receiving ports)}\end{cases} \tag{1.12}$$

where, for a rectangular waveguide of transversal dimensions a and b ($a > b$), $\gamma_{10}=\text{j}\sqrt{k_0^2-(\pi/a)^2}$, with $k_0=2\pi f/c_0$ being the free-space wave number and f the operating frequency, $\mathbf{E}^{inc}=E_0\mathbf{e}_{10}e^{-\gamma_{10}z}$ at the excitation port, and $\mathbf{e}_{10}=\sqrt{2/(a\,b)}\sin(\pi x/a)\,\hat{\mathbf{y}}$.

1.5 Waveguide Port Boundary Condition in the Time Domain

Since our goal is to analyze waveguide discontinuities directly in the TD, we employ the TD representation of the waveguide boundary condition in (1.12), as derived in [6] and [21], using

the inverse Laplace transform (ILT) and applying it for the dominant mode. Before the ILT is applied to (1.12), γ_{10} can be expressed as follows:

$$\gamma_{10} = \mathrm{j}\sqrt{k_0^2 - (\pi/a)^2} = \sqrt{(\pi/a)^2 - k_0^2} = \sqrt{(\pi/a)^2 + (s/c_0)^2}, \quad s = \mathrm{j}\omega \tag{1.13}$$

The ILT of the final equality in (1.13) can be found in [26] and it yields the following TD operator:

$$\Gamma_{10} = \frac{1}{c_0}\frac{\mathrm{d}}{\mathrm{d}t} + h_{10}(t)* \tag{1.14}$$

where * stands for the convolution in the time domain and $h_{10}(t)$ is the impulse response of the dominant waveguide mode, given by

$$h_{10}(t) = \frac{k_{10}}{t} J_1(k_{10}c_0 t)u(t) \tag{1.15}$$

with $k_{10} = \pi/a$, $u(t)$ denoting the unit step function, and J_1 the first-kind Bessel function of the first order. Note that the singular point at $t = 0$ in (1.15) can be avoided by applying L'Hospital's rule and recurrence relation for derivative of the Bessel function $J_n'(z) = [J_{n-1}(z) - J_{n+1}(z)]/2$, where z is the argument of the Bessel function (in this case, $z = k_{10}c_0 t$). Therefore, at $t = 0$, the impulse response of the dominant waveguide mode is equal to $h_{10}(0) = k_{10}^2 c_0/2$. Now, combining expressions in (1.12), (1.14), (1.15), and (1.5), we can incorporate the time-domain boundary condition into the surface integral in (1.10) to obtain

$$G = -\frac{1}{\mu_\mathrm{r}}\left(\frac{1}{c_0}\frac{\mathrm{d}}{\mathrm{d}t} + h_{10}(t)*\right)$$
$$\sum_{j=1}^{N} \alpha_j(t)\left[\oint_{S_1} (\mathbf{n}\times\mathbf{f}_i)\cdot(\mathbf{n}\times\mathbf{f}_j)\mathrm{d}S + \oint_{S_2} (\mathbf{n}\times\mathbf{f}_i)\cdot(\mathbf{n}\times\mathbf{f}_j)\mathrm{d}S\right]$$
$$+\frac{2}{\mu_\mathrm{r}}\left(\frac{1}{c_0}\frac{\mathrm{d}}{\mathrm{d}t} + h_{10}(t)*\right)\oint_{S_1} \mathbf{f}_i\cdot\mathbf{E}^{\mathrm{inc}}\mathrm{d}S, \quad i = 1,2,\ldots N \tag{1.16}$$

where S_1 and S_2 are the surfaces of the waveguide cross sections at the excitation and receiving ports, respectively. Due to the surface integration across the ports, only the unknown coefficients related to the tangential components of the vector basis functions at the ports are taken into account. Note that in (1.16), the TD operator Γ_{10} acts only on time-dependent unknown coefficients and the incident electric field. Substituting (1.16) into (1.8), we obtain the final semi-discretized spatial form of the vector wave equation,

$$[A]\{\alpha(t)\}+\frac{1}{c_0^2}[B]\frac{\mathrm{d}^2\{\alpha(t)\}}{\mathrm{d}t^2}+\frac{1}{c_0\mu_\mathrm{r}}[C]\frac{\mathrm{d}\{\alpha(t)\}}{\mathrm{d}t}+\frac{1}{\mu_\mathrm{r}}[C]\{q_{10}(t)\}=\{f\} \tag{1.17}$$

where the entries of matrices $[C]=[C_1]+[C_2]$, $\{q_{10}(t)\}$, and $\{f\}$ are computed as

$$C_{p_{i,j}}=\oint_{S_p}(\mathbf{n}\times\mathbf{f}_i)\cdot(\mathbf{n}\times\mathbf{f}_j)\mathrm{d}S,\quad p=1,2;\quad i,j=1,2,\ldots N \tag{1.18}$$

$$\{q_{10}(t)\}=h_{10}(t)*\{\alpha(t)\}=\int_0^t h_{10}(t-\tau)\{\alpha(\tau)\}\,\mathrm{d}\tau \tag{1.19}$$

$$\{f\}=\frac{2E_0}{\mu_\mathrm{r}}\left[\frac{1}{c_0}\frac{\mathrm{d}}{\mathrm{d}t}f^{\mathrm{inc}}(t)+h_{10}(t)*f^{\mathrm{inc}}(t)\right]\oint_{S_1}(\mathbf{n}\times\mathbf{f}_i)\cdot(\mathbf{n}\times\mathbf{e}_{10})\mathrm{d}S \tag{1.20}$$

and $f^{\mathrm{inc}}(t)$ stands for the incident pulse function.

1.6 Implicit Unconditionally Stable Time-Stepping Finite Difference Scheme – Newmark-beta Method

Discretization of (1.17) in the TD can be done using different finite-difference schemes. The forward and backward difference approximations are first-order accurate, while the central difference approximation provides second order accuracy. In addition, the forward difference scheme is a numerically unstable method, the backward difference scheme is unconditionally stable, and the central difference scheme is a conditionally stable method, as shown in [1], [6],

[13], and [14]. The most preferable and frequently used time-stepping scheme is the Newmark-beta method, which applies central differences for the first and second derivatives and a weighted average for the undifferentiated quantity [6]. It is shown in [27] that the Newmark-beta method is an implicit unconditionally stable scheme if $\beta \geq 1/4$ (β being the parameter that controls the accuracy and stability of the method). Employing this formulation for $\beta = 1/4$ to discretize (1.17) in the time domain, we obtain

$$\frac{\mathrm{d}^2\{\alpha(t)\}}{\mathrm{d}t^2} = \frac{1}{\Delta t^2}\left[\{\alpha\}^{n+1} - 2\{\alpha\}^{n} + \{\alpha\}^{n-1}\right] \tag{1.21}$$

$$\frac{\mathrm{d}\{\alpha(t)\}}{\mathrm{d}t} = \frac{1}{2\Delta t}\left[\{\alpha\}^{n+1} - \{\alpha\}^{n-1}\right] \tag{1.22}$$

$$\{\alpha(t)\} = \frac{1}{4}\left[\{\alpha\}^{n+1} + 2\{\alpha\}^{n} + \{\alpha\}^{n-1}\right] \tag{1.23}$$

where the discrete-time representation of unknown field coefficients at a time step $t_n = n\Delta t$ is $\{\alpha(t)\} = \{\alpha(n\Delta t)\} = \{\alpha\}^n$. The initial state of the field inside the structure is defined by the causality condition $\{\alpha(t)\} = \{0\}, t \leq 0$, and the convolution integral in (1.19) is discretized using the trapezoidal rule

$$\{q_{10}\}^n = \frac{\Delta t}{2}\left(h_{10}(0)\{\alpha\}^n + h_{10}(t_n)\{\alpha\}^0\right) + \Delta t\sum_{i=1}^{n-1} h_{10}((n-i)\Delta t)\{\alpha\}^i . \tag{1.24}$$

Finally, combining (1.21)–(1.24) yields the following unconditionally stable two-step update scheme:

$$[D_1]\{\alpha\}^{n+1} = \{f\}^n - [D_2]\{\alpha\}^{n-1} - [D_3]\{\alpha\}^n - \frac{1}{\mu_r}[C]\{q_{10}\}^n \tag{1.25}$$

with the $[D]$ matrices being given by

$$[D_1] = \frac{1}{4}[A] + \frac{1}{(c_0\Delta t)^2}[B] + \frac{1}{2\Delta t c_0 \mu_r}[C] \tag{1.26}$$

$$[D_2]=\frac{1}{4}[A]+\frac{1}{(c_0\Delta t)^2}[B]-\frac{1}{2\Delta t c_0\mu_r}[C] \tag{1.27}$$

$$[D_3]=\frac{1}{2}[A]-\frac{2}{(c_0\Delta t)^2}[B]. \tag{1.28}$$

The resultant time-stepping scheme in (1.25) implies that the linear system of equations is solved at each time step, but the matrix $[D_1]$ on the left-hand side of the equation is inverted only once. Also, the discretized version of the impulse response in (1.15), as well as the convolution integral in (1.20), can be precalculated and stored in the memory before the marching in time starts. Unfortunately, the convolution on the left-hand side of (1.25) has to be computed at each time step, which significantly increases the overall simulation time. This problem can be remedied by a truncation of the impulse response in (1.15) or by performing the convolution in the form of a Toeplitz matrix-vector multiplication, as suggested in [21], [28].

1.7 Modal Amplitudes at Waveguide Ports and Scattering Parameters

Once the matrix of unknown electric field coefficients $[\alpha]_{N\times N_t}$ is obtained solving (1.25), these coefficients are substituted back into (1.5), and the modal amplitudes of the dominant mode across the waveguide ports at each time step are calculated using the following expressions:

$$a_{10}(t)=\int_{S_1}\mathbf{e_{10}}\cdot\left[\mathbf{E}(\mathbf{r},t)-\mathbf{E}^{\text{inc}}(\mathbf{r},t)\right]\Big|_{z=z_1}\text{dS}=\int_{S_1}\mathbf{e_{10}}\cdot\mathbf{E}(\mathbf{r},t)\Big|_{z=z_1}\text{dS}\ -\ f^{\text{inc}}(t)\int_{S_1}\mathbf{e_{10}}\cdot\mathbf{e_{10}}\Big|_{z=z_1}\text{dS}\ \text{(at excitation port)},$$

$$b_{10}(t)=\int_{S_2}\mathbf{e_{10}}\cdot\mathbf{E}(\mathbf{r},t)\Big|_{z=z_2}\text{dS}\ \text{(at receiving port)}. \tag{1.29}$$

Finally, the scattering parameters of the structure in Fig. 1.1 are computed as the ratio of the DFT of the modal amplitudes in (1.29), $A_{10}(f_k)$ and $B_{10}(f_k)$, respectively, to the DFT of the excitation pulse signal $F^{\text{inc}}(f_k)$

$$S_{11} = \frac{\mathrm{DFT}\{a_{10}(t_n)\}}{\mathrm{DFT}\{f^{\mathrm{inc}}(t_n)\}} = \frac{A_{10}(f_k)}{F^{\mathrm{inc}}(f_k)} \quad \text{and} \quad S_{21} = \frac{\mathrm{DFT}\{b_{10}(t_n)\}}{\mathrm{DFT}\{f^{\mathrm{inc}}(t_n)\}} = \frac{B_{10}(f_k)}{F^{\mathrm{inc}}(f_k)} \tag{1.30}$$

where the DFT of a function in the time domain can be computed as

$$F(f_k) = F(k) = \sum_{n=0}^{N_\mathrm{f}} f(t_n)\, \mathrm{e}^{-\mathrm{j}\frac{2\pi}{N_\mathrm{f}}nk}, \quad f_k = k\frac{f_\mathrm{s}}{N_\mathrm{f}}, \quad k = 0, 1, \ldots, N_\mathrm{f} - 1, \tag{1.31}$$

with N_f standing for the number of frequency samples (in our case $N_\mathrm{f} = N_\mathrm{t}$) and f_s for the sampling frequency.

1.8 Conclusion

This chapter has proposed a novel higher order and large-domain Galerkin-type FEM for direct 3-D electromagnetic modeling in the time domain and has presented its implementation in the TD-FEM analysis of multiport microwave waveguide devices with arbitrary metallic and dielectric discontinuities. The method is based on the geometrical modeling using Lagrange-type interpolation generalized hexahedra of arbitrary geometrical-mapping orders, field expansion in terms of hierarchical curl-conforming 3-D polynomial vector basis functions of arbitrarily high field-approximation orders, time-stepping with an implicit unconditionally stable finite difference scheme invoking the Newmark-beta method, and mesh truncation introducing the waveguide port boundary condition. Numerical results and validation of the method are presented in the following chapter.

2 TD-FEM – NUMERICAL RESULTS AND DISCUSSION[2]

Numerical examples include transient analysis of a variety of 3-D waveguide structures with metallic and penetrable discontinuities of different shapes, composed of homogeneous and continuously inhomogeneous materials. The results show excellent agreement with indirect numerical solutions obtained from higher order FEM in the frequency domain and alternative full-wave low-order small-domain numerical solutions, as well as with measurements. The emphasis is on the *p*-refinement and convergence properties of the solution, along with conformal geometrical modeling. The examples demonstrate very effective higher order hexahedral meshes constructed from a very small number of large curved conformal finite elements (large domains) and *p*-refined higher-order field expansions, which results in solutions with minimal total number of unknowns.

2.1 Convergence Analysis – Empty Rectangular Waveguide

As the first example, consider a short section of an empty rectangular waveguide, shown in Fig. 2.1. The waveguide section is modeled by means of a single FEM hexahedral element of the first geometrical order ($K_u = K_v = K_w = 1$), which in this case reduces to a brick. Note that this is literally an entire-domain FEM model (an entire computational domain is represented by a single finite element). In order to verify the numerical stability, accuracy, and convergence of the method, the waveguide is analyzed by the higher order TDFEM and the reflection coefficient,

[2] A portion of this chapter (sections 2.1–2.4, 2.7) has been published in *IEEE Transactions on Microwave Theory and Techniques*. © 2013 IEEE. Reprinted, with permission, from N. J. Šekeljić, M. M. Ilić, and B. M. Notaroš, "Higher Order Time-Domain Finite Element Method for Microwave Device Modeling with Generalized Hexahedral Elements," *IEEE Transactions on Microwave Theory and Techniques*, Vol. 61, No. 4, pp. 1425-1434, April 2013.

which theoretically vanishes, is computed in the frequency range from 1.5 GHz to 4.5 GHz. (Note that λ_g = 7.071 cm at f = 4.5 GHz, λ_g being the wavelength of TE_{10} mode).

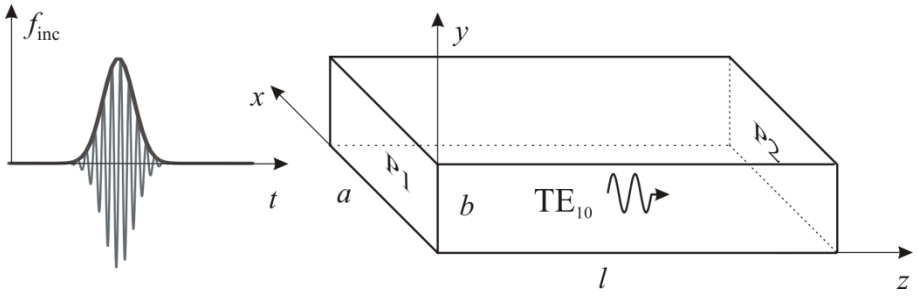

Figure 2.1. Short empty rectangular waveguide section modeled by a single large finite element (literally an entire-domain FEM model) and higher order TDFEM. Dimensions of the waveguide are a = 10 cm, b = 5 cm, and l = 10 cm. © 2013 IEEE.

Polynomial orders of the FEM field expansions are varied from $N_w = 2$ to $N_w = 9$ in the longitudinal waveguide direction whereas they were kept constant, N_u = 6 and N_v = 4, along the longer and shorter waveguide cross-sectional sides, respectively. The waveguide is excited by a modulated Gaussian pulse given by

$$E_0(t) = \mathrm{e}^{-4\left(\frac{t-t_0}{\sigma}\right)^2} \sin\left[2\pi f_c(t-t_0)\right] \text{ V/m} \tag{2.1}$$

where the carrier frequency is $f_c = 3\,\text{GHz}$, half-bandwidth is $\Delta f = 2.5\,\text{GHz}$, $\sigma = 4/(\pi\Delta f)$, and $t_0 = 1.4\sigma$. The parameters of the time-marching process are: the total duration of the time signature T = 10 ns, the total number of time samples N_t = 10,000, and the time step $\Delta t = T/(N_t - 1) \approx 1\,\text{ps}$. The TD vector wave equation (already discretized in space applying the FEM) is solved at each time step using a direct solver, namely, Gaussian elimination. Note that iterative solvers [e.g., a conjugate gradient solver (CGS)] can also be used. In practical cases, the total simulation time or the total duration of the time signature, T, is determined as approximately twice the width of the input signal, which is usually a Gaussian or modulated Gaussian pulse, Neumann pulse (derivative of the Gaussian pulse), or a combination of Gaussian

and Neumann pulses, or based on monitoring the reflections at the input port of the analyzed device [20]. Shown in Fig. 2.2 are the reflection coefficients vs. frequency, computed using (1.30) from the TDFEM solution, for the *p*-refined single-large-element FEM model. The higher order TDFEM results are compared with the two results from [21] where a similar structure is analyzed, but the actual waveguide-section length and time-domain excitation parameters are not specified. The results show a stable behavior, as it is expected because of the Newmark-beta method, and excellent convergence properties with an extreme *p*-refinement. The reflection coefficient obtained by the higher order single-element TDFEM is on average practically equally low (around –75 dB in the given frequency span) as the one obtained by the mixed second order (*h*-refined) model from [21]. Note that the actual results will slightly vary with the choice of the excitation pulse and other parameters in the time-domain analysis (which are not explicitly given in [21]).

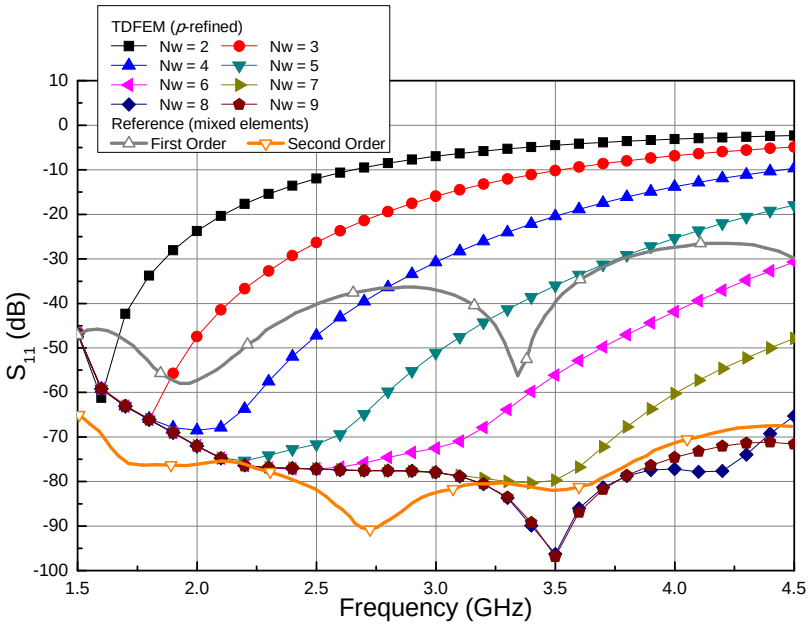

Figure 2.2. Reflection coefficient for the TE_{10} mode in an empty rectangular waveguide in Fig. 2.1: convergence of the higher order TDFEM single-large-element results with *p*-refinement and comparison with the reference (*h*-refined mixed first- and second-order elements) results from [21]. © 2013 IEEE.

Note that the spatial discretization practically does not exist in this example, Fig. 2.1 – the complete computational domain is encompassed by a single finite element. Hence one might wonder, at this point, how a single large finite element can accurately capture the transient response $\mathbf{E}(\mathbf{r},t)$, within the time-stepping solution in the higher order TDFEM, at any point $\mathbf{r}$ in the element and at any time instant t. This is perhaps because the time-domain solutions are intuitively associated [in the spirit of the (most natural and easy to comprehend in TD computations) finite difference time domain (FDTD) method] with the marching in time and space along a very fine grid. In such a grid, the solution at the next grid point (and the next point in time) is obtained by iterating the solution at the present grid point (and the present time) by simultaneously taking a time-marching step Δt and a space-marching step $\Delta u = c\Delta t$ (where u is a chosen spatial coordinate and c is the speed of light in the considered medium). On the other hand, one can easily appreciate that if a single higher order finite element can accurately (and more efficiently than a number of small low-order elements) yield frequency responses (in the context of the FDFEM) within a certain frequency band (beyond which additional *h*- or *p*-refinements are required, as demonstrated in [25]), the same element should equally well carry the same portion of a correctly rendered frequency band contained in a pulse applied as its excitation in the time domain (in the context of the TDFEM). In other words, one might wonder how well the basis functions in the higher order TDFEM are able to approximate generally band-limited (e.g., Gaussian) pulses, typically used in time-domain analyses in practical applications (with band-limited systems). Because this phenomenon is strictly associated with higher order and large-domain FEM modeling in the time domain, and the present study appears to be the first study of such a method, we next present in Fig. 2.3 the least squares approximation of the Gaussian pulse (which is very similar in nature to the Galerkin discretization utilized in our

TDFEM technique) achieved by the higher order polynomial basis functions in (1.7). For the sake of clarity of the presentation, the approximation is shown in one dimension (1-D), along the local parametric (dimensionless) u-coordinate $(-1 \le u \le 1)$ of a single 1-D finite element. The propagating Gaussian pulse is frozen at a time instant at which its peak is supposed to have reached the coordinate u_0, thus its spatial distribution within the element becomes

$$f(u) = \mathrm{e}^{-4(u-u_0)^2/\sigma^2} \tag{2.2}$$

where $\sigma = 4/(\pi \Delta f)$ and $\Delta f = 2$. It can be concluded from the figure that basis functions in (1.7), of order $N_u = 10$ in this example, can indeed approximate the (practically) band-limited Gaussian pulse at any coordinate in the element and at any time instant extremely well. The same, of course, would not hold, with the same accuracy of the approximation, for sharp wideband pulses (e.g., a step function).

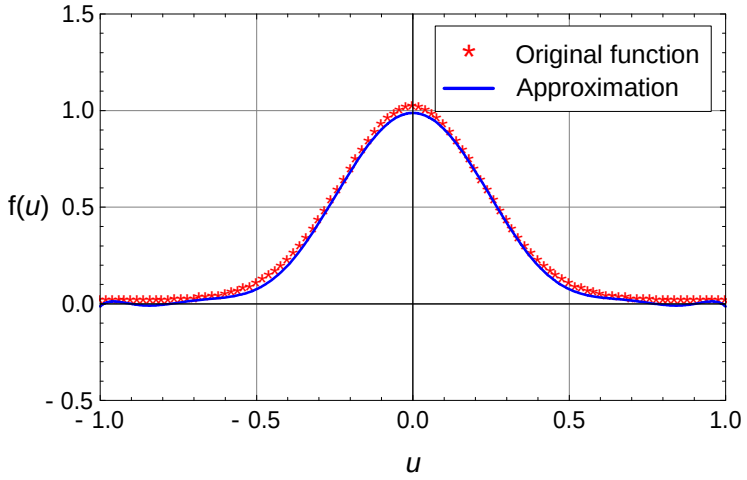

Figure 2.3. Illustration of the higher order polynomial spatial approximation using higher order polynomial basis functions of the Gaussian pulse in (2.2) across a large 1-D finite element. The pulse is frozen at the time instant at which its peak is supposed to have reached the local parametric coordinate $u_0 = 0$.

However, the higher order FEM solutions, being associated with significantly lower numerical dispersion errors [14] (originating from a numerical approximation of the wave propagation

speed in the given medium, which itself is of a limited accuracy) will actually yield better transient responses than the low order small-domain solutions, because the propagating time-domain signals will be less distorted over longer traveling paths and will thus better maintain their original shape.

Shown in Table 2.1 are the computational requirements, in terms of the relative simulation time and memory, for analysis of the waveguide section in Fig. 2.1, for all *p*-refined solutions in Fig. 2.2, with the accuracy of individual solutions being given in Fig. 2.2. In TDFEM simulations, the time marching process requires the maximum memory allocated at any point in time. During this process, the following matrices are allocated: $[D_1]$, $[D_2]$, $[D_3]$, and $[C]$, each of dimension $N \times N$, $[\alpha]$ and excitation matrix $[F]$, defined by (1.20), each of dimension $N \times N_t$, an $1 \times N_t$ array of impulse responses $\{h_{10}\}$, and two $1 \times N$ arrays, $\{q_{10}\}$ and $\{b\}$, where $\{b\}$ is a temporary array in which the right-hand side of the TD equation [(1.15), (1.24), and (1.25)] is stored during one pass through the time marching loop. All computations are carried out without parallelization on an Intel® Core™2 Quad CPU Q6600 at 2.40 GHz 2.39 GHz, with 8 GB RAM, under 64-bit Windows 7 operating system.

Table 2.1. Computational requirements for analysis of the waveguide section in Fig. 2.1 for eight *p*-refined solutions. © 2013 IEEE.

Expansion order, N_w	2	3	4	5	6	7	8	9
Number of unknowns, N	144	197	250	303	356	409	462	515
Relative simulation time	1	1.4	1.77	2.23	2.73	3.2	3.73	4.27
Memory (MB)	22.7	31.3	40.1	49.1	58.3	67.6	77.1	86.8

2.2 Air-Filled WR-90 with Dielectric Post

The second example is an air-filled lossless WR-90 rectangular waveguide with a dielectric post, as shown in Fig. 2.4. The waveguide is operating in the single mode window, hence the proper monomodal modeling is ensured by allowing a certain distance between the discontinuity and the waveguide ports, where the modal amplitudes of the electric field in (1.29) are computed by the higher order TDFEM. The waveguide is excited by the same type of modulated Gaussian pulse as in (2.1), with $f_c = 10\,\text{GHz}$, $\Delta f = 2.5\,\text{GHz}$, $\sigma = 4/(\pi\Delta f)$, and $t_0 = 1.4\sigma$. The large-domain FEM mesh is constructed from only seven hexahedral elements (element dimensions vary from $0.2\lambda_g$ to $1.5327\lambda_g$ at $f = 12$ GHz) with $K_u = K_v = K_w = 1$ and N_u, N_v, and N_w ranging from 4 to 7 in different elements and different directions, which results in a total of 1,791 FEM unknowns.

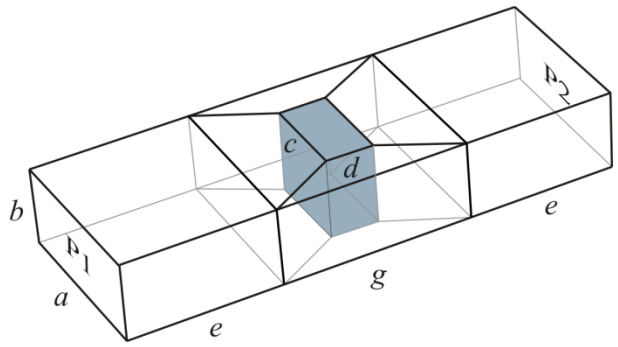

Figure 2.4. WR-90 waveguide with a lossless dielectric ($\varepsilon_r = 8.2$) post and its large-domain hexahedral FEM mesh used in higher order TDFEM computations. Dimensions of the waveguide and mesh elements are $a = 22.86\,\text{mm}$, $b = 10.16\,\text{mm}$, $c = 12\,\text{mm}$, $d = 6\,\text{mm}$, $e = 45.72\,\text{mm}$, and $g = 24\,\text{mm}$. © 2013 IEEE.

The parameters of the time-marching process are T = 10.235 ns, N_t = 5,000, and $\Delta t = 2.047\,\text{ps}$. The obtained transient waveforms, shown in Fig. 2.5, are in an excellent agreement with FDFEM-DFT/IDFT results [24] and in a good agreement with EVFE responses from [29], having in mind that the results in [29] are obtained with a different waveguide excitation (current

probes with no details provided), as opposed to modal excitations in this present work, as well as that no details are provided in [29] about the actual locations of reference planes with respect to which the responses are given. Reflected and transmitted signals exhibit a stable behavior.

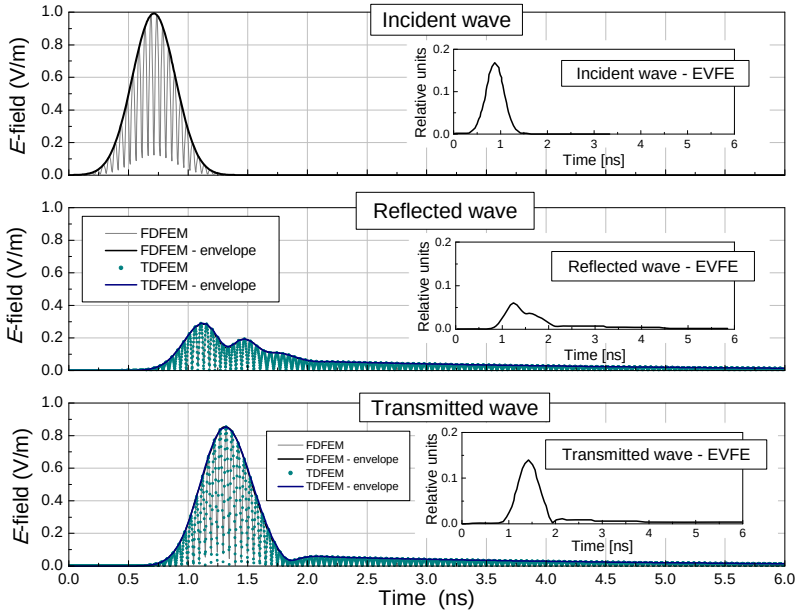

Figure 2.5. Transient waveforms of incident, reflected, and transmitted waves for the structure in Fig. 2.4 and excitation in (2.1) obtained by the higher order TDFEM and FDFEM-DFT/IDFT [24] techniques (note that rectified modulated signals are shown within the envelopes); EVFE results from [29] are shown in figure insets. © 2013 IEEE.

Next, we compute the *S*-parameters at the input and output ports in Fig. 2.4 [using (1.30)]. The sampling frequency is $f_s = 1/\Delta t = 488.52\,\text{GHz}$ (the number of DFT samples is equal to the number of samples in time, $N_f = N_t = 5{,}000$). The higher order TDFEM results are shown in Fig. 2.6, where they are compared with FDFEM results [24] in Fig. 2.6(a) and with FETD (small domain approximation, 72,373 tetrahedral elements, $\Delta x_{\min} = \Delta y_{\min} = \Delta z_{\min} = 1\,\text{mm} \cong \lambda_g/30$, $\Delta t_{\max} = 1.9\,\text{ps}$) [29], EVFE [29], and HFSS (commercial software, direct FD) results in Fig. 2.6(b).

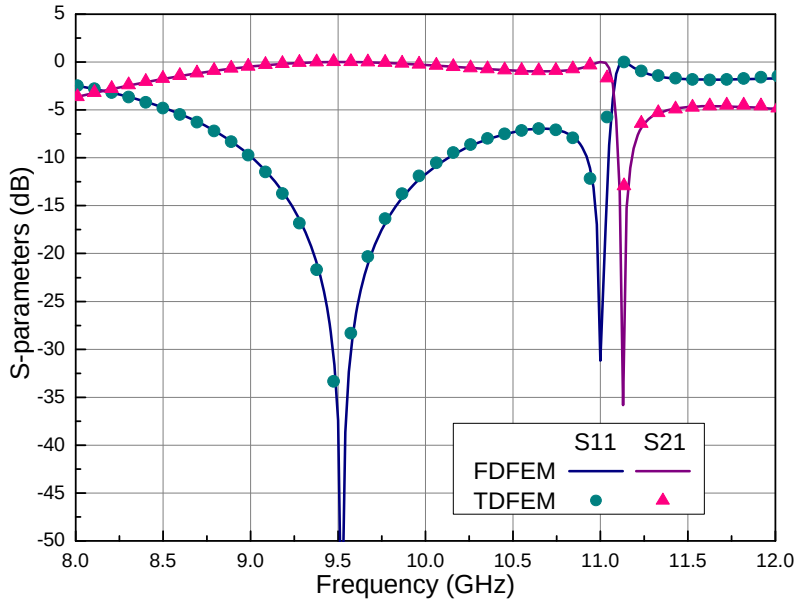

(a)

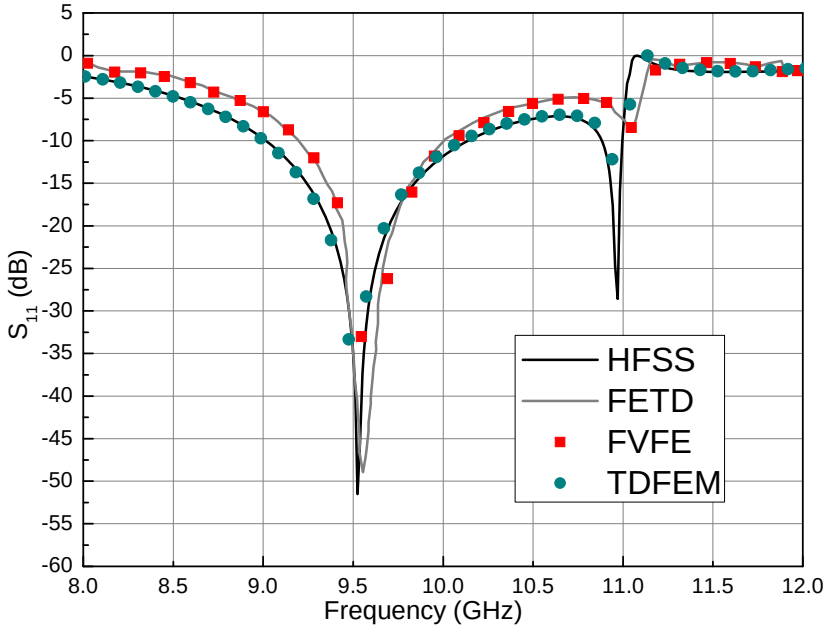

(b)

Figure 2.6. Modal *S*-parameters of the waveguide structure in Fig. 2.4: comparison of higher order TDFEM results with (a) FDFEM results [24] and (b) FETD [29], EVFE [29], and HFSS results. © 2013 IEEE.

It can be concluded based on the figures that TDFEM results practically identically match FDFEM-DFT/IDFT results, as well as that both sets of higher order results match extremely well the reference HFSS results, and in that sense they both outperform the FETD and EVFE results.

2.3 WR-62 with Two Crossed Cylindrical Posts

In the third example, consider a WR-62 waveguide with two crossed metallic cylindrical posts, with the large-domain FEM model shown in Fig. 2.7 (ten generalized hexahedral elements, K_u, K_v, and K_w are 1 or 2, N_u, N_v, and N_w range from 2 to 5, yielding 1,184 unknowns) and the excitation in the form of the signal in (2.1), where $f_c = 14$ GHz and $\Delta f = 3$ GHz. The transient and frequency responses of the structure computed by the higher order TDFEM ($\Delta t = 1.462$ ps and N_t = 5,000) are shown in Fig.2.8. In Fig.2.8(a), we observe an excellent agreement between the TDFEM and FDFEM-DFT/IDFT [24] results for the reflected waveform. In Fig.2.8(b), a very good agreement between the numerical results obtained by the TDFEM, FDFEM [24], and HFSS and the measured data [30] for the S_{11} of the structure is observed.

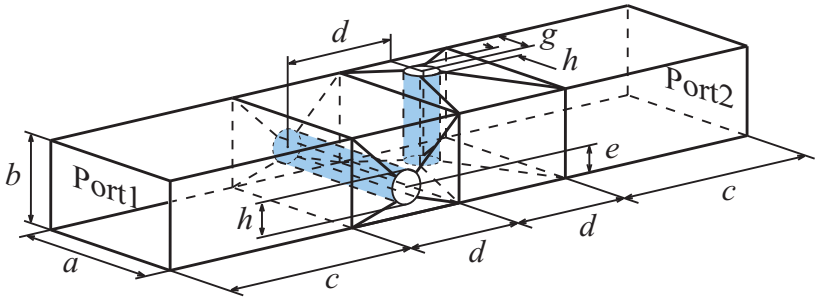

Figure 2.7. Higher order large-domain hexahedral TDFEM model of a WR-62 waveguide with two crossed metallic cylindrical posts (a = 15.7988 mm, b = 7.8994 mm, c = 20 mm, d = 11.51 mm, e = 2.5 mm, g = 4 mm, h = 3 mm). © 2013 IEEE.

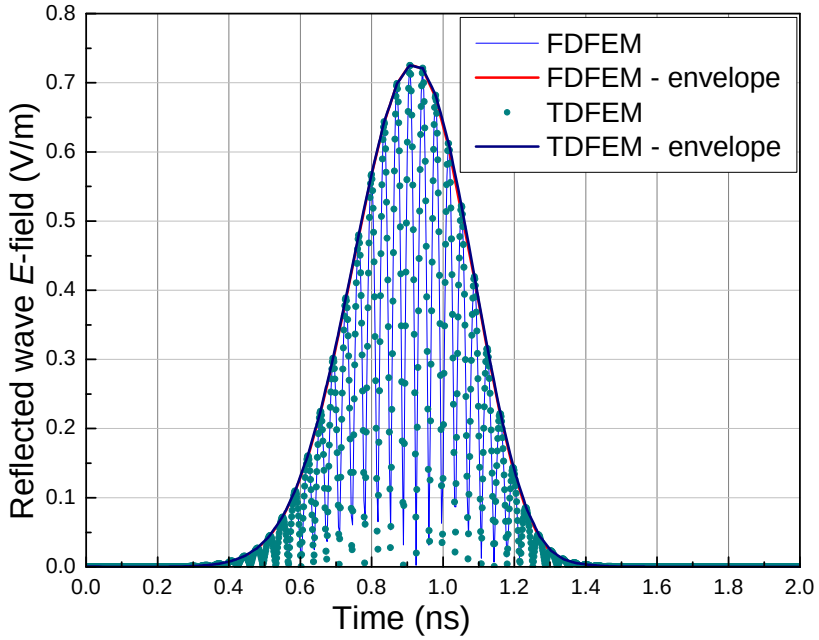

(a)

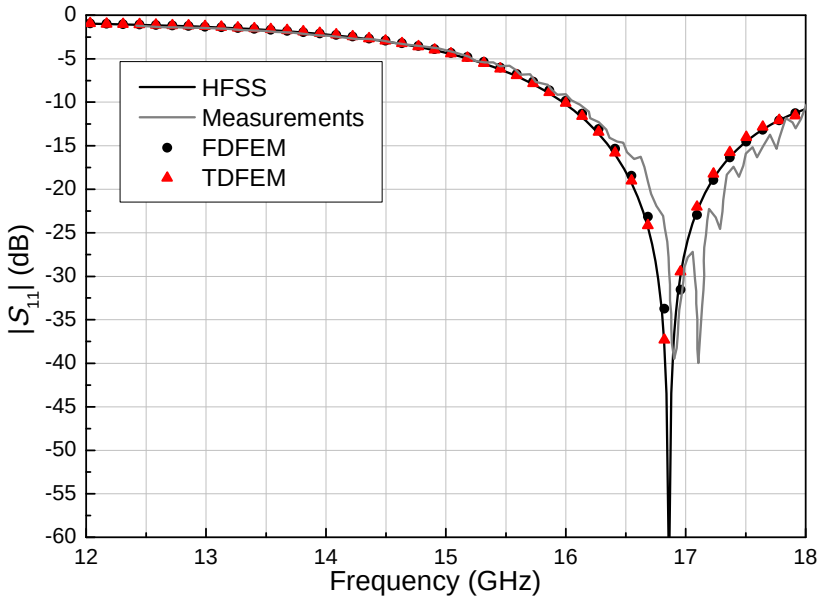

(b)

Figure 2.8. Computed (a) transient and (b) frequency responses for the waveguide structure in Fig. 2.7 using the higher order TDFEM: comparison with FDFEM-DFT/IDFT results [24] in (a) and with FDFEM results [24], HFSS results, and measurements [30] in (b). © 2013 IEEE.

2.4 WR-15 Loaded with Continuously Inhomogeneous Dielectric Slab

As the fourth example, we consider a WR-15 waveguide loaded with a continuously inhomogeneous dielectric slab with a relative permittivity profile given by $\varepsilon_r(u) = 9 - 8u^2$, $-1 < u < 1$ and $u = 2z/c - 1$, as depicted in Fig. 2.9. The transient responses for the reflected wave obtained by the higher order TDFEM [excitation in (2.1), $f_c = 62\,\text{GHz}$, $\Delta f = 15\,\text{GHz}$, $\Delta t = 0.33\,\text{ps}$, and N_t = 5,000] for: (A) an exact continuously inhomogeneous model and (B) an approximate piecewise homogeneous model are shown in Fig. 2.10. Model (A), with the entire slab represented by a single continuously inhomogeneous finite element, consists of only three hexahedral finite elements with $K_u = K_v = K_w = 1$ (one inhomogeneous dielectric element with $N_u = 4$, $N_v = 2$, and $N_w = 7$ and two buffer elements with $N_u = 4$, $N_v = 2$, and $N_w = 4$) and requires only 205 unknowns. Model (B), with the slab approximated by seven homogeneous layers (relative permittivities of layers are given in Fig. 2.9), includes nine hexahedral elements ($K_u = K_v = K_w = 1$, N_u, N_v, and N_w range from 2 to 5) and results in 569 unknowns [24]. The results of the FEM-DFT/IDFT simulations for both models [24] are included for comparison. It can be observed from the figure that in both cases the TDFEM and FEM-DFT/IDFT results are practically identical, as well as that the transient responses for the continuously inhomogeneous model and the seven-layer model agree very well. Note that for model (A), the TDFEM simulation takes 2.5 times less computational time than the FEM-DFT/IDFT simulation, while the TDFEM simulation of model (B) takes 34% more computational time than the FEM-DFT/IDFT simulation. Note also that the FEM-DFT/IDFT solver takes advantage of an extremely fast multifrequency FDFEM analysis of 3-D waveguide structures (the global FEM matrix is filled only once and then reused for every subsequent frequency point) needed for the inverse Fourier transform [24].

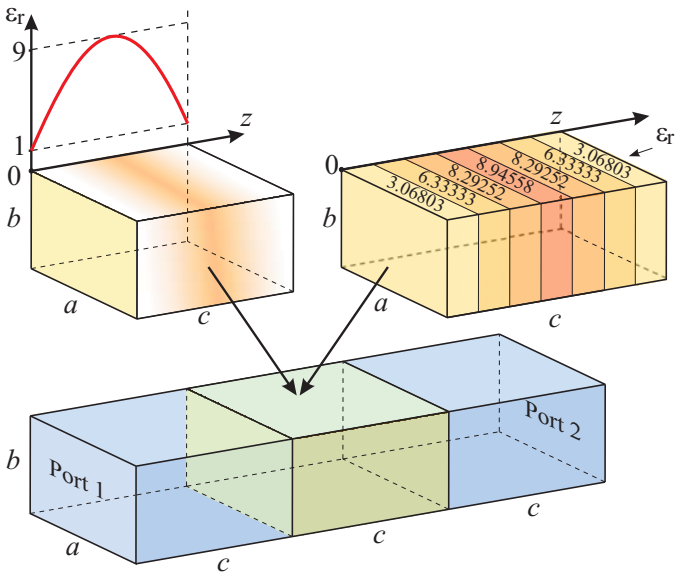

Figure 2.9. Higher order large-domain TDFEM model of a WR-15 waveguide ($a = 3.76$ mm, $b = 1.88$ mm, and $c = 2.5$ mm) with a continuously inhomogeneous (quadratically varying) lossless dielectric load (central element); seven-layer approximate model of the load with piecewise constant approximation of the quadratic permittivity profile [24] is also shown. © 2013 IEEE.

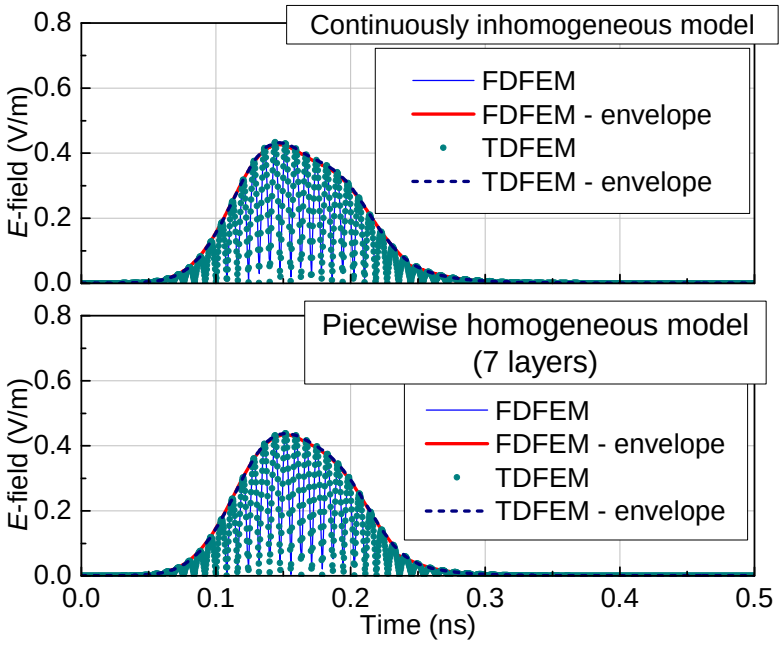

Figure 2.10. Transient response for the reflected wave of the structure in Fig. 2.9: comparison of the higher order TDFEM and FEM-DFT/IDFT [24] results for the exact continuously inhomogeneous model and the approximate piecewise homogeneous model (with seven homogeneous layers), respectively (both models are shown in Fig. 2.9). © 2013 IEEE.

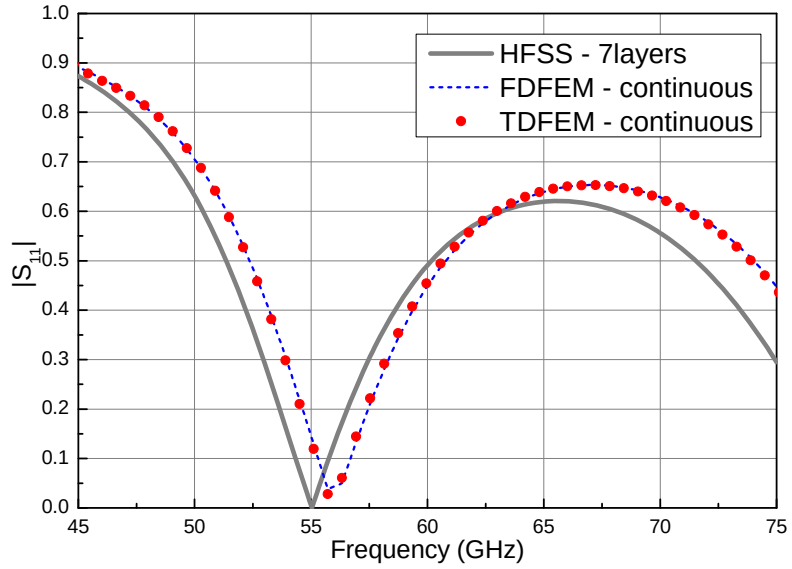

(a)

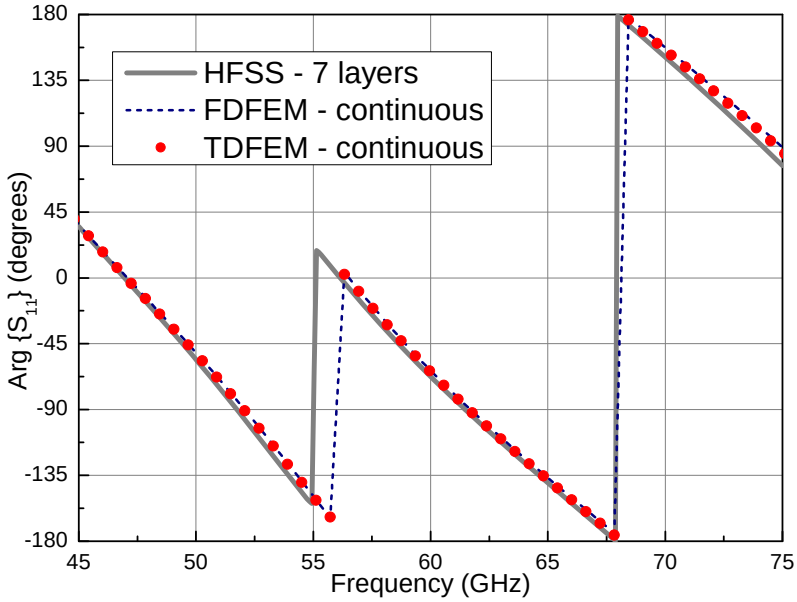

(b)

Figure 2.11. (a) Magnitude and (b) phase (argument) of the S_{11}-parameter of the waveguide structure in Fig. 2.9 obtained by the higher order TDFEM and FDFEM [24], respectively, applied to the exact continuously inhomogeneous model and by HFSS applied to the approximate seven-layer model. © 2013 IEEE.

The computed S_{11}-parameter of the structure in Fig. 2.9 is shown in Fig. 2.11. In the graphs, the TDFEM solution with the continuously inhomogeneous model is compared with the FDFEM solution for the same model and with the HFSS solution for the seven-layer model. We observe

an excellent agreement of the TDFEM and FDFEM-DFT/IDFT results and a very good agreement of both sets of higher order results with the HFSS solution (TDFEM and FDFEM-DFT/IDFT solutions for the seven-layer model, being in an excellent agreement with the HFSS results, are not shown).

2.5 90° *H*-, *E*-Plane WR-75 Bends

In the next example, we analyze 90° *H*- and *E*-plane WR-75 bends with uniform cross-section of dimensions a = 19.05 mm and b = 9.525 mm shown in Fig. 2.12. The radius of the curvature for *H*-band is R_H = 21.6 mm, and for *E*-band R_E = 12 mm, respectively. Both structures are excited with modulated Gaussian pulse given in (2.1) with following parameters: T = 5 ns, Δf = 3 GHz, f_c = 12.5 GHz, N_t = 7000. The bends are modeled with only three large elements of second geometrical order (K = 2) where the maximum size of the elements is approximately one wavelength in the waveguide ($e_{max} \approx \lambda_g$). Note that we used two extra elements of length l = 10 mm, as buffers, in order to assure dominant mode propagation (see Fig. 2.12). In Fig. 2.13, a very good agreement between the numerical results obtained by the higher order TDFEM, reference solution [31], the measured data [31], and excellent agreement with HFSS for the S_{11} of the structure is observed. Our higher order solution is approximated with polynomial orders N = 5, 7 which results in totally 2,108 unknowns while HFSS solution requires 2,293 tetrahedral elements and second order field approximation which results in 14,204 unknowns.

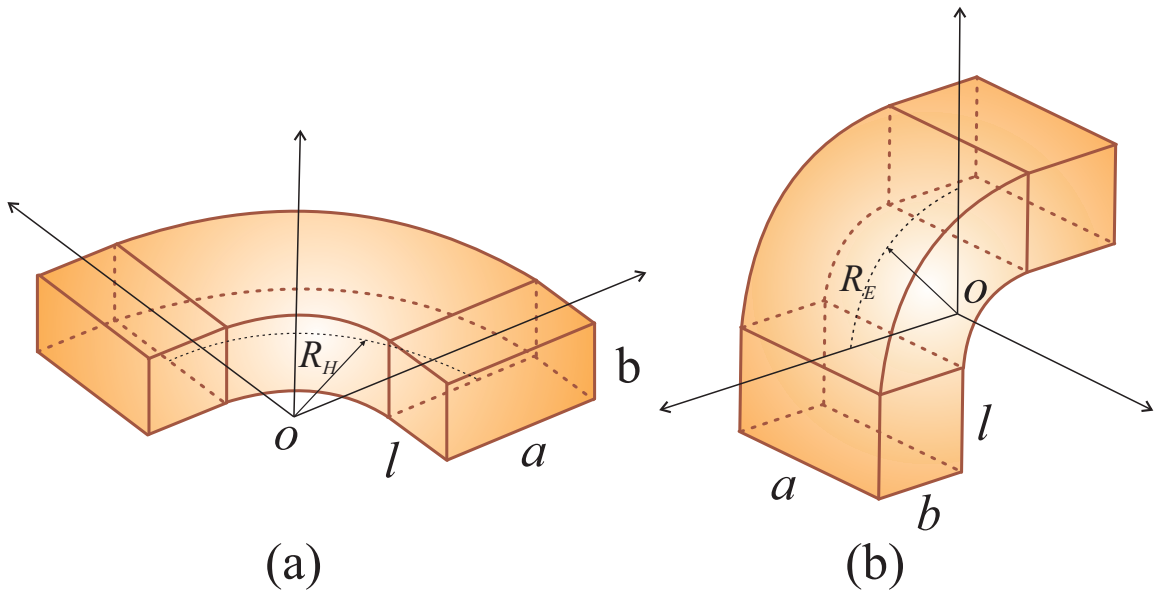

Figure 2.12. Higher order large-domain TDFEM model of 90° (a) *H*-plane and (b) *E*-plane WR-75 bends with uniform cross-section of dimensions a = 19.05 mm and b = 9.525 mm, radius of the curvature for *H*-band is R_H = 21.6 mm, and for *E*-band R_E = 12 mm, respectively, and length of the buffer elements l = 10 mm.

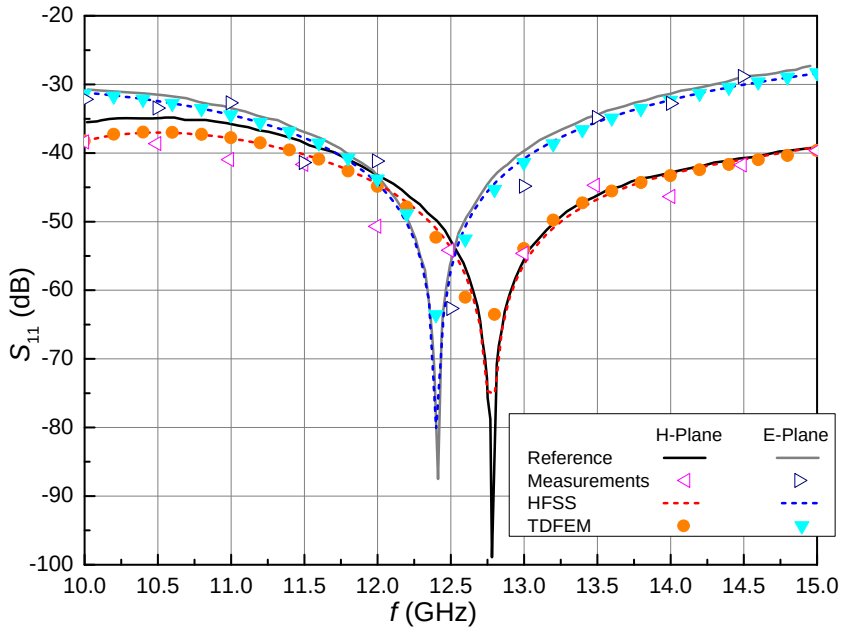

Figure 2.13. Computed frequency responses for the waveguide structures in Fig. 2.12 using the higher order TDFEM: comparison with reference [31], measurements [31], and HFSS results.

2.6 30° Cascaded *H*-Plane WR-90 Bends

As the last example, we perform higher order TDFEM analysis of cascaded 30° *H*-plane, U- and S-type, WR-90 bends with cross-section dimensions a = 22.90 mm, b = 10.20 mm, and mean radius of the curvature R = 15.24 mm, shown in Fig. 2.14. Both models are simulated for two different lengths of the buffer elements: case (i) L = 5 mm, and case (ii) L = 25 mm. Higher order TDFEM model includes only five hexahedral elements (K = 2) as depicted in Fig. 2.14, with maximum dimension $e_{max} = L$ = 25 mm = 1.2 λ_g. The transient responses obtained by the higher order TDFEM [excitation in (2.1), $f_c = 10$ GHz, $\Delta f = 2.5$ GHz, $T = 5$ ns, and N_t = 5,000] for case (i) and case (ii) are shown in Figs 2.15 and 2.16, respectively. Polynomial orders of higher order field expansion vary from N = 4 to N = 7 resulting in 2,050 unknowns.

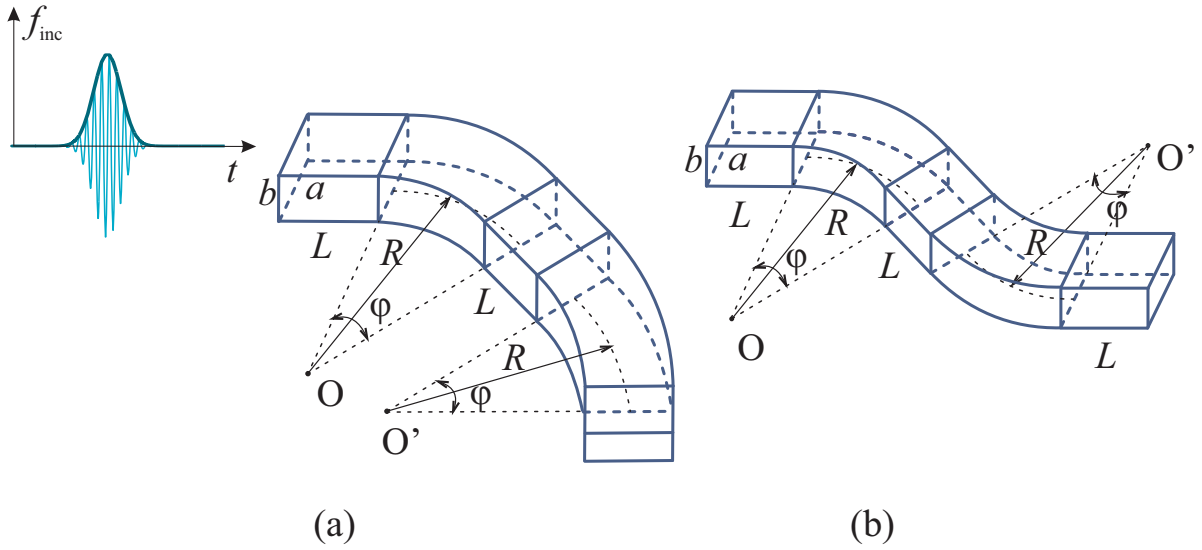

Figure 2.14. Higher order large-domain TDFEM model of cascaded 30° *H*-plane bends (φ = 30°) (a) U-type, (b) S-type with mean radius of the curvature R = 15.24 mm in WR-90 rectangular waveguide with a = 22.90 mm and b = 10.20 mm.

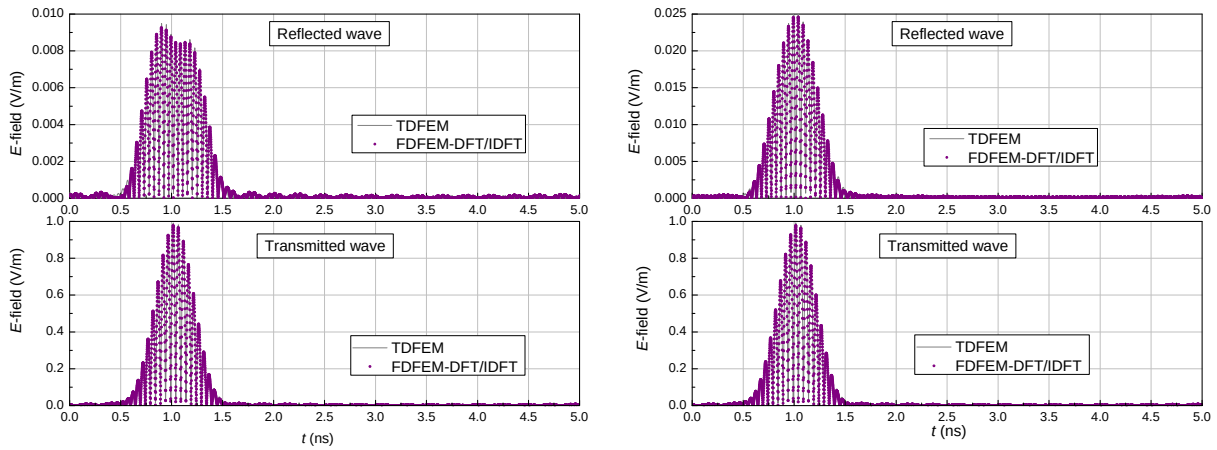

Figure 2.15. Transient response for the reflected and transmitted wave of the structures in Fig. 2.14 (a) U-bend and (b) S-bend: comparison of the higher order TDFEM and FEM-DFT/IDFT [24] results for the case (i) L = 5 mm.

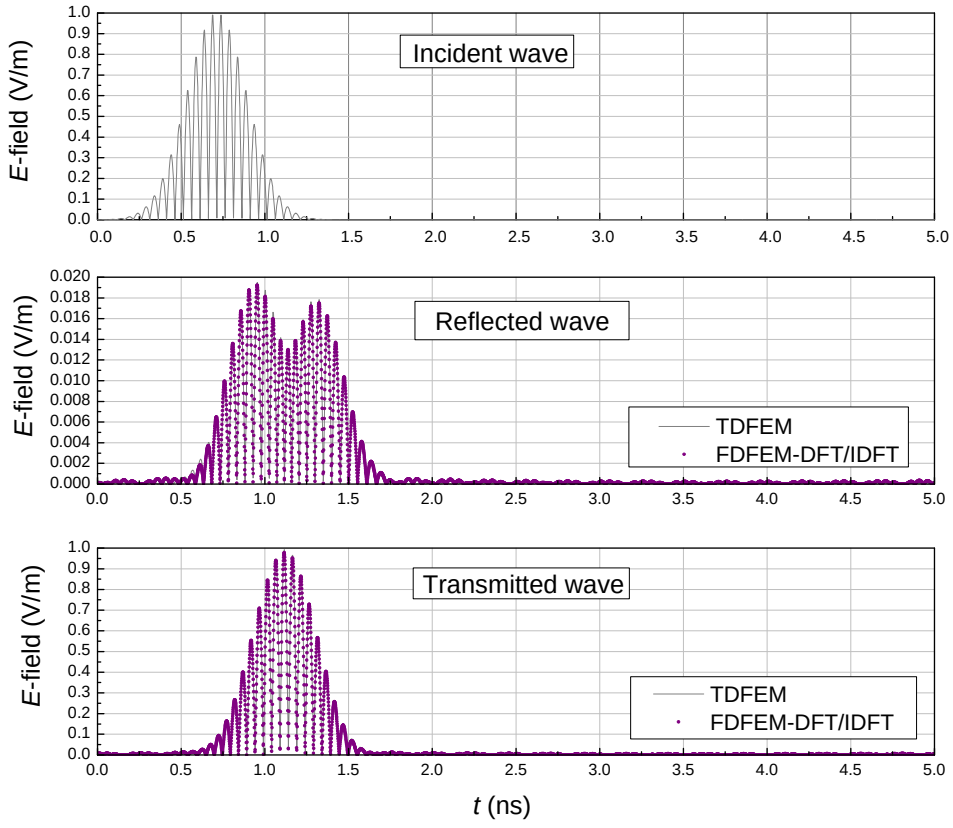

Figure 2.16. Transient response for the incident, reflected and transmitted wave of the structures in Fig. 2.14: comparison of the higher order TDFEM and FEM-DFT/IDFT [24] results for the case (ii) L = 25 mm.

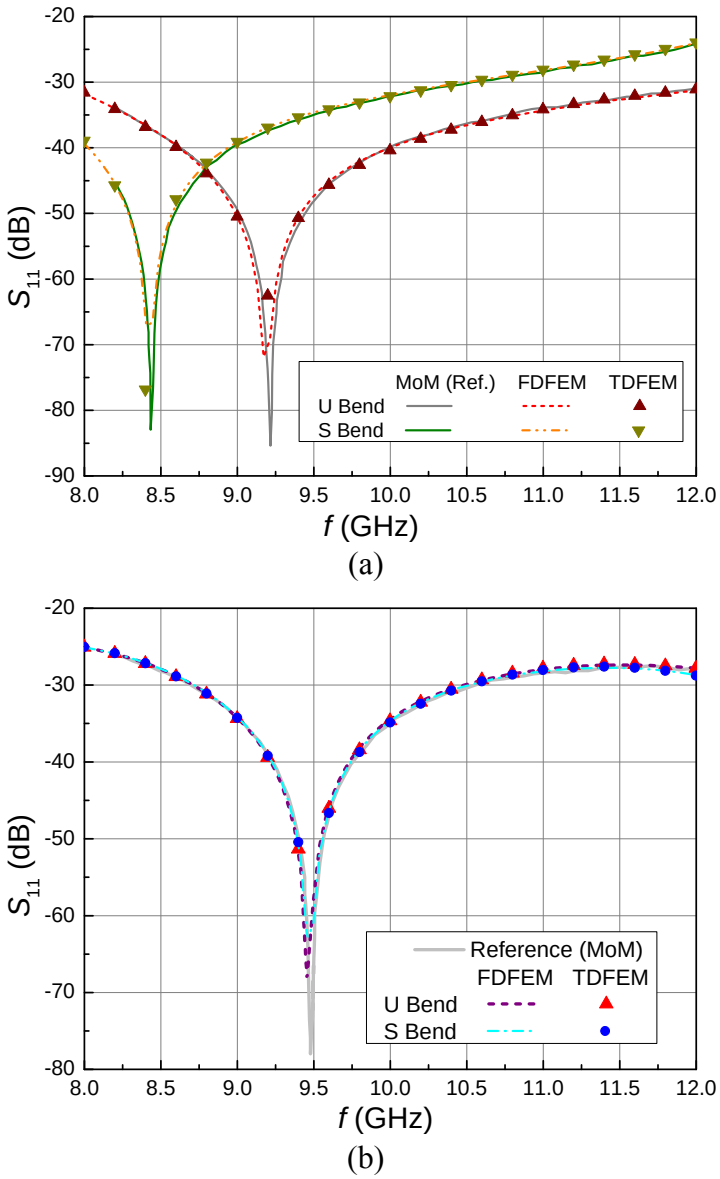

Figure 2.17. Computed frequency responses for the waveguide structures in Fig. 2.14 for (a) case (i) L = 5 mm and (b) case (ii) L = 25 mm using the higher order TDFEM: comparison with MoM reference solution [32], and higher order FDFEM [24].

Reflection coefficient of waveguide structures in Fig. 2.14 is shown in Fig. 2.17, and excellent agreement is observed between three sets of solution: higher order TDFEM and FDFEM [24], and MoM reference solution [32].

As it was expected, sufficiently long separation between curvatures ($L \approx \lambda_g$, case (ii)) ensures that all evanescent modes excited in the junction are significantly attenuated. Therefore, the orientation of the bend is not important and in both structures, U- and S-type bends, we have the same dominant mode propagation (as presented in Fig. 2.16 in time domain, and Fig. 2.17(b) in frequency domain).

2.7 Conclusion

Numerical examples of waveguide structures that include metallic and homogeneous and continuously inhomogeneous dielectric discontinuities have validated the method, which appears to be the first truly higher order 3-D TDFEM technique (the results have demonstrated using field expansions of orders from 2 to 9), and have demonstrated its excellent accuracy, efficiency, stability, convergence, and versatility. They have demonstrated very effective large-domain TDFEM models of 3-D waveguide discontinuities using minimal numbers (from one to ten) of large conformal finite elements and minimal numbers (up to 2,108) of unknowns, which appear to be the first set of large-domain TDFEM modeling examples. The results obtained by the higher order TDFEM are in an excellent agreement with the FDFEM-DFT/IDFT solutions, as well as with measurements and with alternative full-wave numerical solutions in both time and frequency domains.

3 HIGHER ORDER METHOD OF MOMENTS FOR ELECTRIC FIELD INTEGRAL EQUATION MODELING IN TIME DOMAIN[3]

3.1 Introduction

The time domain (TD) surface integral equation (SIE) formulation is an effective approach to transient electromagnetic (EM) analysis of open-region (radiation and scattering) three-dimensional (3-D) structures. TDSIE techniques have two unique advantages as compared to differential equation based numerical approaches, such as the finite element method (FEM), when analyzing homogeneous or piecewise homogeneous radiation and scattering structures in the TD. As SIE based methods, they only require surface discretization of the scatterer and implicitly satisfy radiation boundary condition through Green's functions. As TD methods, they can provide analysis of transient, broadband, and nonlinear phenomena in a single run.

The most explored method in solving TDSIEs is the marching-on-in-time (MOT) method [33]. Several MOT schemes, combined with the method of moments (MoM) Galerkin-type spatial testing, have been developed [34]–[39]. In terms of the numerical properties of proposed and implemented temporal basis functions and their orders, most MOT techniques apply linear approximations of the temporal current expansions [35], [36], [40]–[44]. Higher order Lagrange polynomial temporal basis functions, implemented up to the second order, have been suggested in order to enhance the accuracy of the MOT algorithm [39], [45]–[49].

Novel higher order temporal basis functions derived from Laguerre polynomials are

[3] Material included in this chapter will be published in *IEEE Transactions on Antennas and Propagation:* N. J. Šekeljić, M. M. Ilić, and B. M. Notaroš, "Spatially Large-Domain and Temporally Entire-Domain Electric-Field Integral Equation Method of Moments for 3-D Scattering Analysis in Time Domain," accepted, in print to appear in Vol. 63 No. 6 of *IEEE Transactions on Antennas and Propagation.*

introduced in [50]. These polynomials naturally satisfy the causality condition because they are defined on the interval from zero to infinity (entire-domain temporal basis functions); therefore, they are a desirable choice for transient modeling. By applying the temporal testing procedure in the same fashion as the spatial Galerkin-type testing, and due to the orthogonality of Laguerre polynomials, the temporal variable can be integrated analytically out from the final system of TDSIEs. Instead of the conventional MOT procedure, the final system of equations is solved in marching-on-in-degree (MOD) of temporal basis functions. Like implicit MOT schemes [38], the MOD approach does not have to satisfy the Courant-Friedrich-Levy (CFL) sampling criterion relating the spatial to the temporal discretization. The MOD scheme employing weighted Laguerre polynomials as temporal bases has been implemented within different MoM-SIE formulations in the TD, including the electric field integral equation (EFIE), magnetic field integral equation (MFIE), and combined field integral equation (CFIE) formulations, for transient scattering analysis of conducting and dielectric structures [51]–[58]. Compared to the implicit MOT scheme, which results in a sparse system matrix and where the sparsity/stability depends on the size of the time step, the MOD scheme produces a full system matrix independent of the time step/order of the time-variant basis functions. The minimal order of the Laguerre polynomials for the temporal support is defined by the time duration and frequency bandwidth product of an incident wave [51], [53]. Finally, the Laguerre polynomials decay to zero at infinite time, thus the solution cannot become oscillatory for late times.

In terms of the numerical properties of proposed and implemented spatial basis functions and their orders, however, practically all the existing MOT and MOD 3-D MoM-TD SIE simulation tools for EM scattering analysis are low-order or small-domain (subdomain) techniques, with the EM structure being modeled by planar triangular surface elements that are electrically very small

and the electric and magnetic currents over the elements are approximated by the first-order spatial basis functions, namely, Rao-Wilton-Glisson (RWG) functions [59]. This results in a very large number of spatial unknowns (unknown current-distribution coefficients) needed to obtain results of satisfactory accuracy, with all the associated problems and large requirements in computational resources. In addition, flat triangular patches do not provide enough flexibility and efficiency in modeling of structures with pronounced curvature.

An alternative approach – constituting the higher order or large-domain (sometimes also referred to as the entire-domain) computational EM [25] – is based on using higher order basis functions defined on large curved geometrical elements (patches) [60], which can greatly reduce the number of unknowns for a given problem and enhance the accuracy and efficiency of the computation. However, this approach seems to have not been fully employed in the MoM-TD SIE analysis yet; namely, almost none of the reported MoM-MOT/MOD TD SIE results and applications in the literature demonstrate actual using and implementation of spatial discretization models with current approximation orders higher than one (higher order modeling). Moreover, for MoM-TD SIE modeling of general structures that may possess arbitrary curvature, it is convenient to have both higher order geometrical flexibility for curvature modeling and higher order current-approximation flexibility for spatial current modeling – in the same method. Also, it is convenient to use hierarchical higher order bases, which allow elements of different orders and sizes combined together in the same model. Notable examples of spatially higher order MoM-MOT TD SIE modeling are the boundary integral equation (BIE) method in the TD using isoparametric curvilinear quadratic approximation of geometry and both spatial and temporal dependence of fields [61], [62] and the higher order Calderon preconditioned EFIE TD solver employing Graglia-Wilton-Peterson

(GWP) divergence- and quasi curl-conforming (DQCC) spatial basis functions of up to third order on second-order curvilinear triangular elements [63]. Another example are spatially higher order vector basis functions (up to the second order) in conjunction with band-limited interpolatory functions (BLIFs) for temporal discretization have been introduced in [37]. In addition, none of the works employ large elements (or a combination of large and small elements) in the MoM-TD SIE model (large-domain modeling).

This research proposes a novel spatially large-domain and temporally entire-domain MoM-TD EFIE method, with full temporal and spatial Galerkin testing, for 3-D transient EM analysis of conducting scatterers based on higher order geometrical modeling and current expansion and MOD scheme. The geometry of the structure is modeled using Lagrange-type interpolation generalized quadrilaterals of arbitrary geometrical-mapping orders and the spatial current distributions over the elements are expanded in terms of hierarchical divergence-conforming polynomial vector basis functions of arbitrarily high current-approximation orders [60]. Note that the quadrilateral elements have been chosen to facilitate surface meshes that can employ very large elements, which is consistent with the large-domain modeling and higher order current expansion paradigm. Triangular elements could be used (with appropriate local parent coordinate systems) but with limited flexibility in terms of large-domain modeling. Time variations of the currents are expressed by orthogonal entire-domain temporal basis functions derived from Laguerre polynomials and the transient response of the scatterer is obtained by an iterative solution of the final system of spatially and temporally discretized MoM-TD EFIE equations in a MOD fashion [58]. It should be noted that the MOD is a particularly suitable choice here since the focus of this paper is on higher order spatial elements. However, MOD has seen limited use

in literature because its efficiency may often be considerably weaker than with the methods that use local basis functions in time, e.g., [63].

To the best of our knowledge, this dissertation presents the first MoM-TD SIE method with very high spatial and temporal expansion orders (the results demonstrate using current expansions of spatial orders from 2 to 8 and geometrical-mapping orders from 1 to 4 in conjunction with using higher order, entire-domain Laguerre polynomial temporal basis functions) and the first set of spatially large-domain MoM-TD SIE modeling examples (the electrical sizes of flat and curved patches in models are up to about 1.7 wavelengths at the maximum frequency in the frequency spectrum of the pulse excitation). The new method is also the first MoM-MOD method with spatially higher order expansions.

3.2 EFIE Formulation in TD

Consider a 3-D conducting, nonpenetrable (PEC – perfect electric conductor) body excited by an incident wave (e.g., a Gaussian pulse or its derivative), as shown in Fig. 3.1.

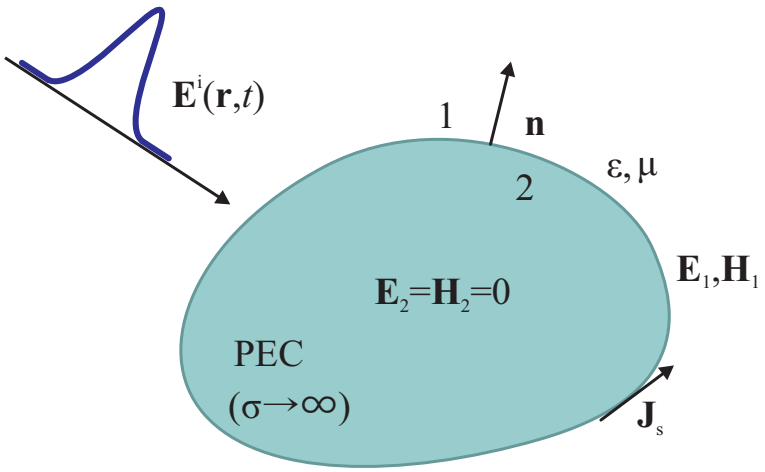

Figure 3.1. 3-D PEC scatterer excited by an incident Gaussian pulse – analysis by the MoM-MOD TD EFIE method.

The total tangential electric field (superposition of incident field $\mathbf{E}_{\mathrm{i}}$ and scattered field $\mathbf{E}$) on the boundary surface S is equal to zero at each time instant,

$$[\mathbf{E}(\mathbf{r},t)]_{\mathrm{tang}} + (\mathbf{E}_{\mathrm{i}}(\mathbf{r},t))_{\mathrm{tang}} = 0, \quad \mathbf{r} \in S, \quad (\forall)\, t \geq 0\,. \tag{3.1}$$

The scattered electric field in the unbounded homogeneous background medium of permittivity ε and permeability μ is expressed in terms of surface electric current density vector $\mathbf{J}_{\mathrm{S}}$ over S as follows:

$$\mathbf{E}(\mathbf{r},t) = -\frac{\partial \mathbf{A}(\mathbf{r},t)}{\partial t} - \nabla\Phi(\mathbf{r},t)\,. \tag{3.2}$$

The Lorentz (retarded) potentials are given by

$$\mathbf{A}(\mathbf{r},t) = \frac{\mu}{4\pi}\int_S \frac{\mathbf{J}_{\mathrm{S}}(\mathbf{r}',t-R/c)}{R}\,\mathrm{d}S\,, \tag{3.3}$$

$$\Phi(\mathbf{r},t) = \frac{1}{4\pi\,\varepsilon}\int_S \frac{\rho_{\mathrm{S}}(\mathbf{r}',t-R/c)}{R}\,\mathrm{d}S = -\frac{1}{4\pi\,\varepsilon}\int_S \int_0^{t-R/c} \frac{\nabla_{\mathrm{s}}\cdot\mathbf{J}_{\mathrm{S}}(\mathbf{r}',t')}{R}\,\mathrm{d}t'\mathrm{d}S\,, \tag{3.4}$$

where $R = |\mathbf{r}-\mathbf{r}'|$ represents the distance between the observation point $\mathbf{r}$ and the source point $\mathbf{r}'$, $\tau = t - R/c$ is the time (delay) that the EM wave travels from the source to the observation point, and c is the intrinsic speed of propagation of the EM wave in the background medium. Note that in (3.4), the surface charge density ρ_{s} is related to $\mathbf{J}_{\mathrm{S}}$ based on the continuity equation, $\nabla_{\mathrm{s}}\cdot\mathbf{J}_{\mathrm{S}} = -\partial\rho_{\mathrm{S}}/\partial t$. Having in mind the integral expressions for scattered electric field $\mathbf{E}$ in (3.2)–(3.4), (3.1) represents the TD EFIE for $\mathbf{J}_{\mathrm{S}}$ as unknown, which is discretized and solved using the MoM with Galerkin testing in space-time in conjunction with the MOD scheme [56], [57].

3.3 Geometrical Modeling using Higher Order Quadrilateral Surface Elements

The geometry of the structure in Fig. 3.1 is modeled by means of generalized curved quadrilateral patches shown in Fig. 3.2 and analytically described as [60]

$$\mathbf{r}(u,v) = \sum_{k=0}^{K_u} \sum_{l=0}^{K_v} \mathbf{r}_{kl} \Lambda_k^{K_u}(u) \Lambda_l^{K_v}(v), \quad -1 \le u, v \le 1, \tag{3.5}$$

where K_u and K_v (K_u, $K_v \ge 1$) are geometrical orders of the element along u and v parametric coordinates, respectively (note that the orders do not need to be the same within an element), $\mathbf{r}_{kl}$ are constant vector coefficients related to position vectors of the interpolation nodes, see Fig.3.2, $\Lambda(u)$ represent Lagrange interpolation polynomials in the u coordinate,

$$\Lambda_k^{K_u}(u) = \prod_{\substack{j=0 \\ j \ne k}}^{K_u} \frac{u - u_j}{u_k - u_j}, \tag{3.6}$$

with the nodes defined as $u_j = (2j - K_u)/K_u$, $j = 0,1,...,K_u$, and similarly for $\Lambda(v)$. Usually, the equidistant distribution of interpolation nodes along each coordinate in parametric space is used. Of course, the use of specific nonequidistant node distribution, which would provide additional modeling flexibility and accuracy in some applications, is possible as well. Note that the 3-D generalization of the quadrilateral in Fig. 3.2 is used in the higher order FEM-TD method [64].

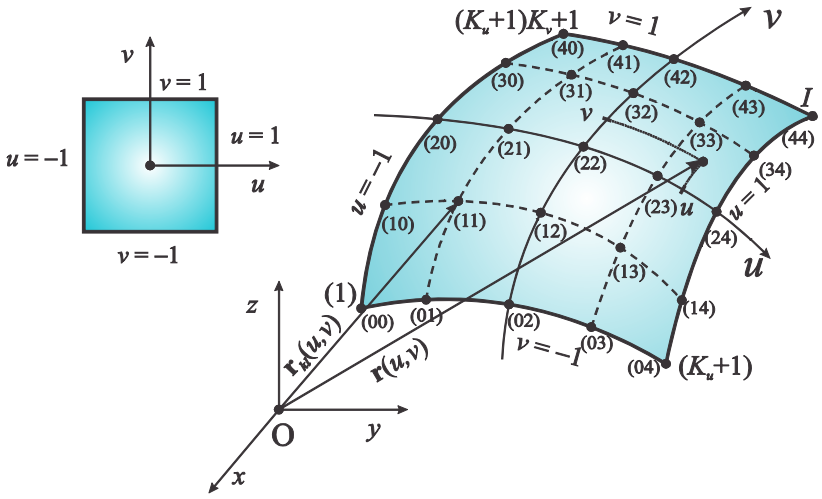

Figure 3.2. Generalized curved parametric quadrilateral MoM-SIE patch defined by (3.5), with the square parent domain.

3.4 Higher Order Temporal and Spatial Basis Functions

In the novel MoM-TD EFIE method, the time-variant electric current density and the accompanying surface charge density over every generalized quadrilateral in the model are expanded using temporal and spatial higher order basis functions as follows:

$$\mathbf{J}_S(\mathbf{r},t)=\frac{\partial \mathbf{h}(\mathbf{r},t)}{\partial t}\,,\qquad \rho_S(\mathbf{r},t)=-\nabla\cdot\mathbf{h}(\mathbf{r},t)\,, \tag{3.7}$$

$$\mathbf{h}(u,v,t)=\sum_{i=0}^{N_u}\sum_{j=0}^{N_v-1}h_{uij}(t)\,\mathbf{f}_{uij}(u,v)+\sum_{i=0}^{N_u-1}\sum_{j=0}^{N_v}h_{vij}(t)\,\mathbf{f}_{vij}(u,v) \tag{3.8}$$

where **h** is the Hertz vector introduced as the actual unknown in the MoM solution procedure in order to avoid temporal integration in (3.4) [65], [53], and u and v are local parametric coordinates of an element (SIE patch) in the model [see Eq. (3.5)]. Unknown time-dependent coefficients in (3.8) associated with the u-component of the Hertz vector h_{uij} are expanded using a linear combination of the three associated Laguerre functions with successive orders,

$$h_{uij}(t)=\sum_{q=0}^{M}h_{uij,q}\left(\Psi_q(st)-2\Psi_{q+1}(st)+\Psi_{q+2}(st)\right) \tag{3.9}$$

(time-dependent coefficients associated with *v*-component of the Hertz vector h_{vij} can be expanded in a similar fashion). Here, *M* is the order of temporal basis functions, *s* is the scaling factor which controls the accuracy of the temporal support, $h_{uij,q}$ are unknown constant coefficients, $\Psi_q(st) = \mathrm{e}^{-st/2} L_q(st)$, $t \geq 0$, are associated Laguerre temporal basis functions, and $L_q(st)$ are Laguerre polynomials of order *q* and argument $x = st$, defined as

$$L_q(x) = \frac{\mathrm{e}^x}{q!} \frac{\mathrm{d}^q}{\mathrm{d}x^q}(x^q \mathrm{e}^{-x}), \quad q \geq 0,\, x \geq 0\,. \tag{3.10}$$

These polynomials satisfy the following recursive relation:

$$\begin{aligned} &L_0(x) = 1, \quad L_1(x) = 1 - x, \\ &L_q(x) = \frac{1}{q}((2q - 1 - x)L_{q-1}(x) - (q-1)L_{q-2}), \quad q \geq 2. \end{aligned} \tag{3.11}$$

Linear combination of weighted Laguerre polynomials, (3.9), is suggested in [56], [58] in order to improve the computational efficiency as compared to the conventional MOD method where the time-dependent part of the Hertz vector is expanded only by a single associated Laguerre function set $\Psi_q(st)$ [53], [55], [57]. The Laguerre polynomials have excellent causality, orthogonally, recursive-computation, and convergence properties [56], and are extremely convenient for the purpose of temporal expansions in the large-domain MoM-TD EFIE method. Functions $\mathbf{f}$ in (3.8) are higher order hierarchical-type divergence-conforming spatial basis functions defined on each generalized quadrilateral patch (see Fig. 3.2). For the local *u*- and *v*-components of the Hertz vector, they are given by [60]

$$\begin{aligned} &\mathbf{f}_{uij}(u,v) = \frac{P_i(u)v^j}{\Im(u,v)}\mathbf{a}_u(u,v), \\ &\mathbf{f}_{vij}(u,v) = \frac{u^i P_j(v)}{\Im(u,v)}\mathbf{a}_v(u,v), \end{aligned} \qquad P_i(u) = \begin{cases} 1-u, & i = 0 \\ u+1, & i = 1 \\ u^i - 1, & i \geq 2, \text{even} \\ u^i - u, & i \geq 3, \text{odd} \end{cases}, \quad -1 \leq u, v \leq 1\,. \tag{3.12}$$

(see Fig. 3 in [66] for visualization of these functions). Parameters N_u and N_v in (3.8) are the adopted degrees of the spatial polynomial approximation of the Hertz vector. The unitary vectors $\mathbf{a}_u$ and $\mathbf{a}_v$ in (3.12) are obtained as $\mathbf{a}_u(u,v) = \partial\mathbf{r}(u,v)/\partial u$ and $\mathbf{a}_v(u,v) = \partial\mathbf{r}(u,v)/\partial v$, with $\mathbf{r}$ given in (3.5), and $\Im$ is the Jacobian of the covariant transformation, $\Im(u,v) = |\,\mathbf{a}_u(u,v) \times \mathbf{a}_v(u,v)\,|$. Furthermore, we consider the functions in the following simplified form:

$$\mathbf{f}_{uij}(u,v) = \frac{\Gamma_{ij}(u,v)}{\Im(u,v)}\frac{\partial\mathbf{r}(u,v)}{\partial u}, \qquad \mathbf{f}_{vij}(u,v) = \frac{\Gamma_{ij}(u,v)}{\Im(u,v)}\frac{\partial\mathbf{r}(u,v)}{\partial v}, \tag{3.13}$$

where Γ are the simple 2-D power functions,

$$\Gamma_{ij}(u,v) = u^i v^j . \tag{3.14}$$

Note that the lowest order of approximation ($N_u = N_v = 1$) yields the rooftop functions on generalized quadrilateral patches (which, for such basis functions, then must be very small).

Substituting (3.2)–(3.4) combined with (3.7)–(3.9) into (3.1) and applying the analytical expressions for the second derivative of the time dependent part of the Hertz vector h_{ij} (h_{ij} representing either h_{uij} or h_{vij}),

$$\frac{\mathrm{d}^2 h_{ij}(t)}{\mathrm{d}t^2} = \sum_{q=0}^{M} \frac{s^2}{4} h_{ij,q}\left(\Psi_q(st) + 2\Psi_{q+1}(st) + \Psi_{q+2}(st)\right), \tag{3.15}$$

with the first time-derivative being due to the magnetic vector potential term in (3.2) and the second due to the substitution of the surface current distribution in terms of the Hertz vector (3.7), the TDEFIE formulation can be finally expanded using unknown coefficients $h_{ij,q}$ and higher order temporal and spatial basis functions Ψ and $\mathbf{f}$, respectively, as follows:

$$\left[\frac{\mu s^2}{4\pi}\sum_{i=0}^{N_u}\sum_{j=0}^{N_v-1}\sum_{q=0}^{M}\left(h_{uij,q} + 2h_{uij,q-1} + h_{uij,q-2}\right)\int_S \frac{1}{4R}\Psi_q(s\tau)\mathbf{f}_{uij}(\mathbf{r}')\mathrm{d}S - \frac{\nabla}{4\pi\varepsilon}\sum_{i=0}^{N_u}\sum_{j=0}^{N_v-1}\sum_{q=0}^{M}\left(h_{uij,q} - 2h_{uij,q-1} + h_{uij,q-2}\right)\int_S \frac{1}{4R}\Psi_q(s\tau)\nabla'_s\cdot\mathbf{f}_{uij}(\mathbf{r}')\mathrm{d}S\right.$$
$$\left. + \frac{\mu s^2}{4\pi}\sum_{i=0}^{N_u-1}\sum_{j=0}^{N_v}\sum_{q=0}^{M}\left(h_{vij,q} + 2h_{vij,q-1} + h_{vij,q-2}\right)\int_S \frac{1}{4R}\Psi_q(s\tau)\mathbf{f}_{vij}(\mathbf{r}')\mathrm{d}S - \frac{\nabla}{4\pi\varepsilon}\sum_{i=0}^{N_u-1}\sum_{j=0}^{N_v}\sum_{q=0}^{M}\left(h_{vij,q} - 2h_{vij,q-1} + h_{vij,q-2}\right)\int_S \frac{1}{4R}\Psi_q(s\tau)\nabla'_s\cdot\mathbf{f}_{vij}(\mathbf{r}')\mathrm{d}S\right]_{\mathrm{tang}} = (\mathbf{E}_{\mathrm{i}}(\mathbf{r},t))_{\mathrm{tang}}.$$

(3.16)

The closed form of the second derivative of the time dependent part of the Hertz vector (3.15) is derived satisfying the properties of Laguerre polynomials, i.e., causality and orthogonality [56], [67]. The error due to a finite difference approximation of this derivative, used in traditional MOT methods, is eliminated utilizing the analytical expression. In addition, there is no need for temporal interpolation of the solution. Once unknown coefficients are obtained, the current/field distribution over the SIE element can be computed at any instant in time. Note that in (3.16), when compared to (3.9) and (3.15), the terms inside the temporal summation are regrouped with respect to unknown coefficients $h_{ij,q}$ instead of associated Laguerre functions Ψ_q.

3.5 Full Time-Space MoM Galerkin Testing

The TDEFIE (3.16) is tested by means of the full temporal and spatial Galerkin method [25], [60], [38] i.e., using the same functions used for current (Hertz-vector) expansion. The generalized Galerkin impedances corresponding, respectively, to the magnetic vector potential and electric scalar potential terms in the expression for the scattered field **E** in (3.2) in the model can be derived, using (3.3) and (3.4), in the following form:

$$Z^{A}_{mn,pq} = \frac{\mu}{4\pi}\int_{S_m}\int_{S_n}\int_{sR/c}^{\infty}\frac{1}{R}\mathbf{f}_m(u_m,v_m)\cdot\mathbf{f}_n(u_n,v_n)\Psi_p(st)\Psi_q(s\tau)\,\mathrm{d}(st)\,\mathrm{d}S_n\,\mathrm{d}S_m\,, \tag{3.17}$$

$$Z^{\Phi}_{mn,pq} = \frac{1}{4\pi\varepsilon}\int_{S_m}\int_{S_n}\int_{sR/c}^{\infty}\frac{1}{R}\big(\nabla\cdot\mathbf{f}_m(u_m,v_m)\big)\big(\nabla\cdot\mathbf{f}_n(u_n,v_n)\big)\Psi_p(st)\Psi_q(s\tau)\,\mathrm{d}(st)\,\mathrm{d}S_n\,\mathrm{d}S_m \tag{3.18}$$

where Ψ_p and Ψ_q are, respectively, the temporal testing and basis functions, p and q are indices/orders of the temporal testing and basis support, and $\mathbf{f}_m$ and $\mathbf{f}_n$ are the spatial testing and basis functions on the mth and nth generalized quadrilateral elements (S_m and S_n). The impedance in (3.18) is obtained applying the surface divergence theorem and the property of higher order

divergence conforming functions that the normal component of the testing function $\mathbf{f}_m$ is either zero at the element edges or the two contributions of the elements sharing an edge exactly cancel out in the final expressions for generalized impedances. The source-to-field distance R in (3.17) and (3.18) is computed as $R = |\mathbf{r}_m(u_m, v_m) - \mathbf{r}_n(u_n, v_n)|$, with $\mathbf{r}$ being defined in (3.5).

Due to causality and orthogonality of Laguerre polynomials [56], temporal integrals in (3.17) and (3.18) can be handled analytically first, resulting in the two types of Green's functions for 2-D spatial integrals, as follows

$$\begin{aligned} I_{pq}(sR/c) &= \int_{sR/c}^{\infty} \Psi_p(st)\,\Psi_q(st - sR/c)\,\mathrm{d}(st) \\ &= \begin{cases} \mathrm{e}^{-sR/(2c)}, & q = p \\ \mathrm{e}^{-sR/(2c)}(L_{p-q}(sR/c) - L_{p-q-1}(sR/c)), & q < p \\ 0, & q > p. \end{cases} \end{aligned} \tag{3.19}$$

Taking into account the parametric representation of the quadrilateral surface element, in (3.5), and simplified representation of the spatial basis functions in (3.13) and (3.14), generalized impedance terms in (3.17) and (3.18) corresponding to the testing functions defined by indices i_m and j_m on the mth quadrilateral and the basis function defined by indices i_n and j_n on the nth quadrilateral become

$$Z^{A,i}_{mn,pq}(i_m, j_m, i_n, j_n) = \sum_{k_m=1}^{K_u^{(m)}} \sum_{l_m=0}^{K_v^{(m)}} \sum_{k_n=1}^{K_u^{(n)}} \sum_{l_n=0}^{K_v^{(n)}} k_m k_n \mathbf{r}_{kl}^{(m)} \cdot \mathbf{r}_{kl}^{(n)} \cdot \xi_i\,(i_m + k_m - 1, j_m + l_m, i_n + k_n - 1, j_n + l_n), \tag{3.20}$$

$$\begin{aligned} &Z^{\Phi,i}_{mn,pq}(i_m, j_m, i_n, j_n) = i_m i_n \xi_i\,(i_m - 1, j_m, i_n - 1, j_n), \\ &i_m = 0, 1, \ldots, N_u^{(m)},\ j_m = 0, 1, \ldots, N_v^{(m)},\ i_n = 0, 1, \ldots, N_u^{(n)},\ j_n = 0, 1, \ldots, N_v^{(n)},\ i = 1, 2. \end{aligned} \tag{3.21}$$

In these equations, $N_u^{(m)}$ and $N_v^{(m)}$ are the Hertz-vector approximation orders of the mth quadrilateral along the u- and v-coordinate, respectively, $N_u^{(n)}$ and $N_v^{(n)}$ are the corresponding orders for the nth quadrilateral, and the integration limits in both quadrilaterals are $u_1 = v_1 = -1$ and $u_2 = v_2 = 1$. In addition, $K_u^{(m)}$ and $K_v^{(m)}$ are the geometrical orders along the u- and v-

coordinate, respectively, $\mathbf{r}_{kl}^{(m)}$ are the geometrical vector coefficients in the polynomial expansion of the mth quadrilateral, $K_u^{(n)}$, $K_v^{(n)}$, and $\mathbf{r}_{kl}^{(n)}$ are the corresponding geometrical parameters for the nth quadrilateral in the model, and ξ_i is the basic Galerkin potential integral given by

$$\xi_i(i_m, j_m, i_n, j_n) = \int_{u_{1m}}^{u_{2m}} \int_{v_{1m}}^{v_{2m}} \int_{u_{1n}}^{u_{2n}} \int_{v_{1n}}^{v_{2n}} u_m^{i_m} v_m^{j_m} u_n^{i_n} v_n^{j_n} g_i(R)\, \mathrm{d}u_n\, \mathrm{d}v_n\, \mathrm{d}u_m\, \mathrm{d}v_m, \quad i = 1, 2 \,. \tag{3.22}$$

The ξ_1-type integral [for $i = 1$ in (3.22)], involving the first Green's function based on (3.19), $g_1(R) = I_{pq}(sR/c)/\mathrm{R} = \mathrm{e}^{-sR/(2c)}/R$, when $q = p$, has a $1/R$-type singularity, which is taken care of as in our frequency-domain (FD) MoM-SIE methods [25], [60]. The ξ_2-type integral [for $i = 2$ in (3.22)], with the second Green's function $g_2(R) = I_{pq}(sR/c)/\mathrm{R} = \mathrm{e}^{-sR/(2c)}(L_{p-q}(sR/c) - L_{p-q-1}(sR/c))/R$ when $q < p$, is not singular for R approaching zero, since $\lim_{R \to 0} g_2(R) = -s/c$; this can be proved by applying L'Hospital's rule and properties of the Laguerre polynomials.

The generalized Galerkin voltages, namely, the column-matrix elements due to the incident field on the right-hand side of the equation (3.16), are evaluated, after the temporal and spatial Galerkin testing, as

$$V_{m,p}^{\mathrm{i}} = \int_{S_m} \mathbf{f}_m \cdot \int_{t=0}^{\infty} \Psi_p(st)\, \mathbf{E}^{\mathrm{i}}(\mathbf{r}, t)\, \mathrm{d}(st)\, \mathrm{d}S_m \,. \tag{3.23}$$

In order to compute the temporal integral in (3.23) numerically, the upper limit is truncated to a finite duration of the time-domain signature T_{f} multiplied by the scaling factor s, ensuring that all further transient variations in the spatial domain of interest can be neglected.

Finally, the generalized Galerkin impedances corresponding to the complete set of spatial basis functions in (3.12) can be obtained as a linear combination of those in (3.20) and (3.21), corresponding to the simplified functions in (3.13) and (3.14), and similarly for the generalized

voltages, which greatly expedites the matrix fill process when compared to the direct computation of final impedances and voltages [60]. Moreover, the Galerkin impedances and voltages for any higher order set of basis functions of divergence-conforming polynomial type can also be constructed as a linear combination of the impedances for the simple 2-D power functions in (3.13) and (3.14).

3.6 MOD Solution of MoM-TD EFIE

After Galerkin testing of (3.16) in space-time, with all generalized impedance and voltage matrices in (3.20)–(3.23) being already precalculated, the global system of linear algebraic equations can be obtained in the following form:

$$
\begin{aligned}
&[Z_{mn}]\{h_{n,p}\} = \{V^{\mathrm{i}}_{m,p}\} - [Z^{A,1}_{mn}](2\{h_{n,p-1}\} + \{h_{n,p-2}\}) - [Z^{\Phi,1}_{mn}](\{h_{n,p-2}\} - 2\{h_{n,p-1}\}) \\
&- \sum_{q=0}^{p-1} [Z^{A,2}_{mn,M-p+q}](\{h_{n,q}\} + 2\{h_{n,q-1}\} + \{h_{n,q-2}\}) - \sum_{q=0}^{p-1} [Z^{\Phi,2}_{mn,M-p+q}](\{h_{n,q}\} - 2\{h_{n,q-1}\} + \{h_{n,q-2}\}), \qquad (3.24) \\
&p = 0,1,...,M, \quad q = 0,1,...,p-1, \quad m = 1,2,...,N_{\mathrm{MoM}}, \quad n = 1,2,...,N_{\mathrm{MoM}},
\end{aligned}
$$

where $[Z_{mn}]=[Z^{A,1}_{mn}]+[Z^{\Phi,1}_{mn}]$ is the system matrix, which takes into account contributions of the generalized impedance matrices, from (3.20) and (3.21) (for $[Z^{A,1}_{mn}]$ and $[Z^{\Phi,1}_{mn}]$, respectively), for the ξ_1-type integral from (3.22) combined with (3.19) for the cases when $q = p$. As can be seen, the system matrix does not depend on the orders of temporal testing and basis functions, p and q, respectively; therefore, it is computed and inverted only once. Generalized impedances (3.20) and (3.21) corresponding to the ξ_2-type integral, with (3.22) combined with (3.19) for the cases when $q < p$, are precalculated for each combination of the temporal testing and basis function indices, p and q, and stored in 3-D matrices constituted by M-element arrays of 2-D matrices $[Z^{A,2}_{mn,k}]$ and $[Z^{\Phi,2}_{mn,k}]$, $k = M - p + q$, of size $m \times n = N_{\mathrm{MoM}} \times N_{\mathrm{MoM}}$, with M being the order of

temporal basis functions and N_{MoM} the total number of MoM spatial unknowns. The minimal order M is defined by the time duration, T_{f}, and the frequency bandwidth, B, of the excitation so that $M \geq 2BT_{\mathrm{f}} + 1$ [51], [53]. Finally, the system (3.24) is solved recursively in the marching-on-in-degree (MOD) fashion for unknown coefficients of the Hertz vector $\{h_{n,p}\}$, $n = 1, 2, \ldots, N_{\mathrm{MoM}}$, $p = 0, 1, 2, \ldots, M$. Note that, comparing (3.24) with (3.16), the temporal summation on the right-hand side of the system equation (which includes already known coefficients) is done up to $p - 1$ instead of M because of the property (3.19), $I_{pq}(sR/c) = 0$ when $q > p$. Note also that initial coefficients for $p = 0$, $\{h_{n,0}\}$, are obtained as the solution of the matrix equation $[Z_{mn}]\{h_{n,0}\} = \{V^{\mathrm{i}}_{m,0}\}$. In this case, the only contribution from the right-hand side of the system (3.24) is due to the excitation vector $\{V^{\mathrm{i}}_{m,0}\}$, while all other terms are equal to zero because of the causality property of Laguerre polynomials. The system of equations (3.24) for the pth order is solved by Gaussian elimination for unknown coefficients $\{h_{n,p}\}$. By postprocessing of the obtained coefficients, the current $\mathbf{J}_{\mathrm{s}}$ over any generalized quadrilateral patch in the model is computed using (3.7), where the first derivative of $h_n(t)$ is calculated analytically as

$$\frac{\mathrm{d}h_n(t)}{\mathrm{d}t} = \sum_{q=0}^{M} \frac{s}{2} h_{n,q}\left(\Psi_q(st) - \Psi_{q+2}(st)\right) \tag{3.25}$$

Computation of electric and magnetic fields due to $\mathbf{J}_{\mathrm{s}}$, as well as of any other quantity of interest for the analysis, is then straightforward.

3.7 Conclusion

This dissertation has proposed a novel spatially large-domain and temporally entire-domain method of moments for EFIE modeling of 3-D conducting scatterers in the time domain. The

method uses higher order geometrical elements in the form of curved Lagrange interpolation generalized quadrilateral patches, higher order spatial current expansions based on hierarchical divergence-conforming polynomial vector basis functions, temporal current modeling by means of orthogonal weighted associated Laguerre basis functions, full temporal and spatial Galerkin testing, and MOD scheme for an iterative solution of the final system of spatially and temporally discretized MoM-TD EFIE equations. This chapter has presented theoretical background, development, and implementation of all major numerical components of the new method. Detailed validation of the method can be found in chapter 4.

4 TD-MOM – NUMERICAL RESULTS AND DISCUSSION[4]

In this chapter, six PEC scattering structures in free space are analyzed to validate and evaluate the proposed spatially large-domain and temporally entire-domain MoM-MOD TD EFIE method. In all the examples, we solve for the induced transient surface current densities, as the most rigorous representative of the solution accuracy, critical for all near field parameters and quantities. Generally, the accuracy of far field computations is much better than that for the current distribution. All the structures are illuminated by an incident Gaussian pulse as shown in Fig. 4.1 and given by

$$\mathbf{E}_{\mathrm{i}}(\mathbf{r},t) = \mathbf{E}_0 \frac{4}{T_{\mathrm{w}}\sqrt{\pi}} \mathrm{e}^{-\gamma^2}, \quad \gamma = \frac{4}{T_{\mathrm{w}}}(c_0 t - c_0 t_0 - \mathbf{r}\cdot\hat{\mathbf{k}}), \tag{4.1}$$

where the vector amplitude $\mathbf{E}_0$ takes into account the polarization of the wave, $\hat{\mathbf{k}}$ is the unit vector in the propagation direction of the incident wave, $\mathbf{r}$ is the position vector of the observation point with respect to the global coordinate origin, c_0 is the speed of light, t_0 represents a time delay of the Gaussian peak from the time origin, and T_{w} is the width of the Gaussian pulse. Time units in the examples are expressed in terms of light meters (lm), $t\,[\mathrm{lm}]=c_0 t$.

[4] A portion of this chapter (sections 4.2–4.7) will be published in *IEEE Transactions on Antennas and Propagation:* N. J. Šekeljić, M. M. Ilić, and B. M. Notaroš, "Spatially Large-Domain and Temporally Entire-Domain Electric-Field Integral Equation Method of Moments for 3-D Scattering Analysis in Time Domain," accepted, in print to appear in Vol. 63 No. 6 of *IEEE Transactions on Antennas and Propagation.*

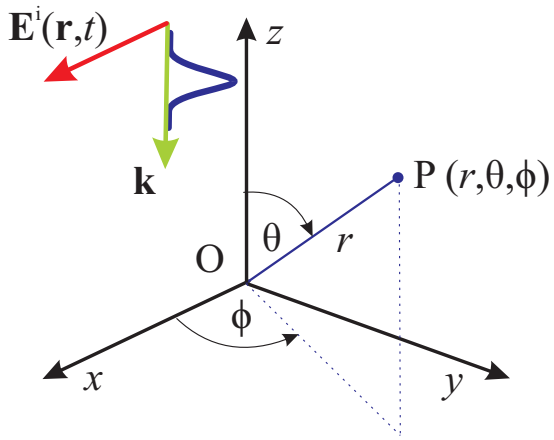

Figure 4.1. Incident Gaussian pulse defined in (4.1) (shown for $\mathbf{E}_0 = E_0\hat{\mathbf{x}}$ and $\hat{\mathbf{k}} = -\hat{\mathbf{z}}$) and associated spherical coordinate system defining elevation and azimuthal angles, θ and ϕ, respectively – as excitation of conducting scatterers analyzed by the MoM-MOD method.

4.1 1-D Preliminary Results – Scattering from a Wire Scatterer

The preliminary results given in the first example demonstrate very good accuracy and convergence properties of TD MoM-MOD method on a simple 1-D scattering model. Consider a thick wire scatterer along z-axis of length L = 2 m and radius a = 12.5 mm illuminated by a Gaussian pulse (4.1) with E_0 = 1 V/m, T_w = 1 lm, and t_0 = 3 lm at different angles of incidence with respect to z-axis. Spatial distribution of the current along the wire is approximated with rooftop basis functions ($N_u = N_v = 1$) while for the temporal dependence in the method, we adopt M = 90. In Fig. 4.2, computed current distribution at f = 300 MHz, is presented for different incident angles: $\theta = 90^o$ (normal incidence) and $\theta = 30^o, 75^o$ (oblique incidence). TD-MoM results in conjunction with DFT are compared with FD-MoM results, and we observe an excellent agreement of the two sets of MoM results.

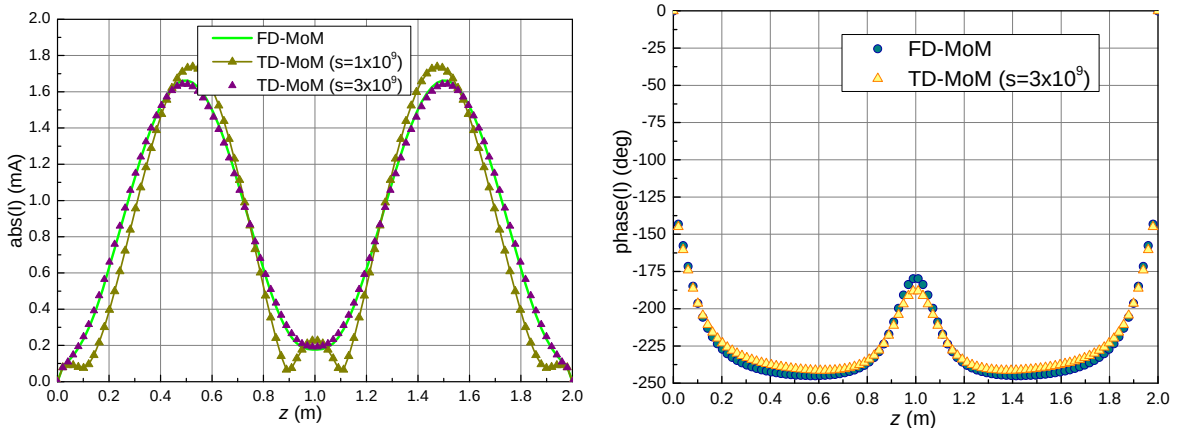

(a)

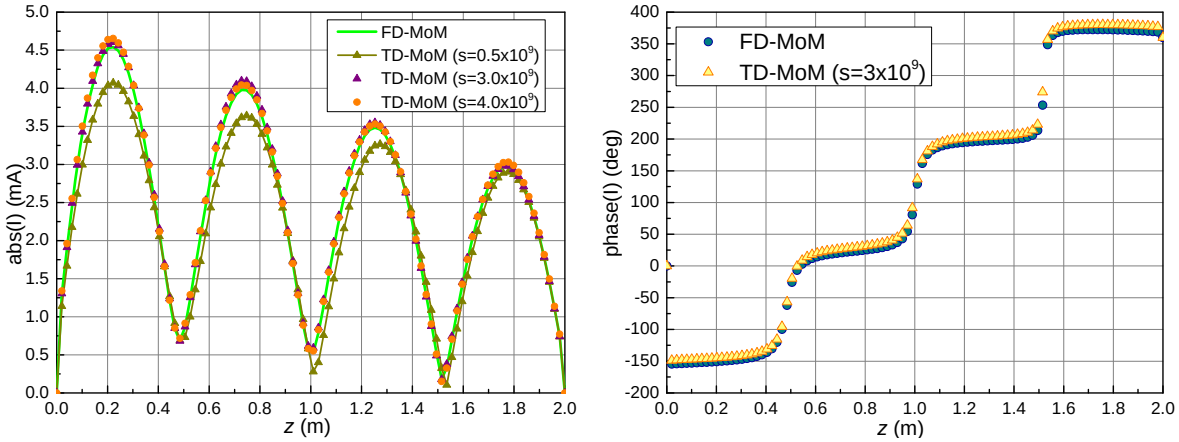

(b)

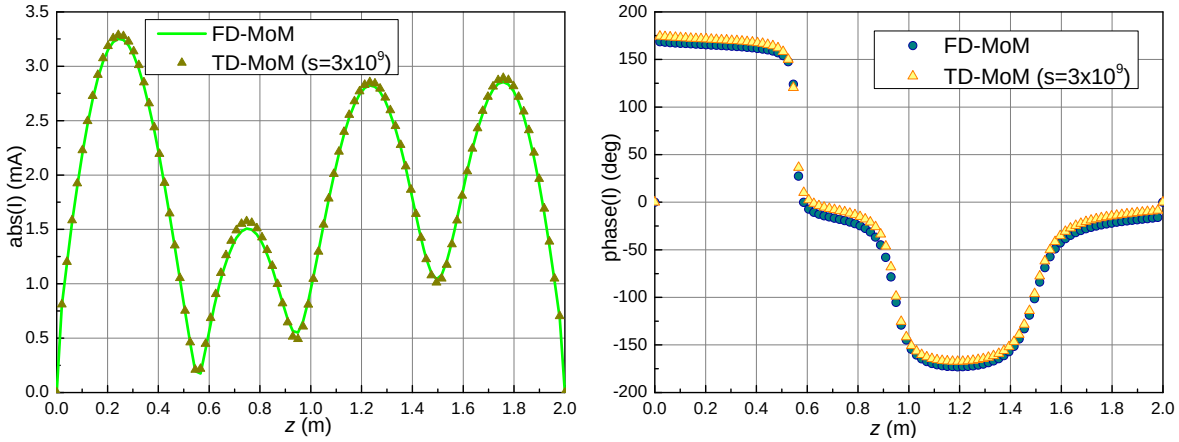

(c)

Figure 4.2. Current distribution (magnitude and phase) along the wire scatterer at f = 300 MHz, for three angles of incidence: (a) $\theta = 90^{o}$, (b) $\theta = 30^{o}$, and (c) $\theta = 75^{o}$.

4.2 Convergence Analysis – Square Plate

As the next example, we perform the convergence analysis of the new MoM-MOD method for a metallic square plate with edge length $a = 2$ m. Excitation is by a Gaussian pulse (Fig. 4.1) normally impinging on a plate with $E_0 = 1$ V/m, $T_w = 4$ lm, and $t_0 = 6$ lm. The wave is linearly polarized with its electric field vector being parallel to one pair of plate edges. We consider in all examples that the pulse has significant spectral components up to f_{max} where the spectral amplitude decays to 0.1% of the maximal value. In this example it is approximately $f_{max} = 250$ MHz. We consider two models of the first geometrical order ($K_u = K_v = K = 1$) for the plate scatterer: (A) plate subdivided into 3 × 3 equal square SIE elements, of electrical size $e_A = a/3 = 0.556\lambda$ (λ being the free-space wavelength) at f_{max}, and (B) entire-domain model of the plate with a single SIE element, of electrical size $e_B = a = 1.667\lambda$ at f_{max} [note that even e_A in model (A) is approximately six times larger than the size of elements used in low-order small-domain MoM techniques, $e_{small\text{-}domain} \approx 0.1\lambda$]. First, we investigate the optimal order of temporal basis functions, varying M in model (A) from 10 to 80, for a fixed order of spatial basis functions $N_u = N_v = N = 4$ (an overly safe choice based on our study of higer order parameters for the MoM-FD SIE method in [68]), which results in a total of $N_{MoM} = 264$ spatial unknowns, and a fixed scaling factor $s = 10^9$. Fig. 4.3(a) shows that $M = 30$ is sufficient for accurate results. Next, shown in Fig. 4.3(b) is the p-refinement of model (B), with N ranging from 2 to 5, for the fixed order of temporal current approximation $M = 30$ and scaling factor $s = 10^9$, so chosen to provide accurate transient solution. Note that parameters M and s are the same as for model (A); as expected, they are not influenced by the size of the element, only parameter N is. The higher order results are compared with a low-order MoM-MOT solution [45], which includes 112 flat triangular patches and 153 spatial unknowns (the surface current density is approximated using

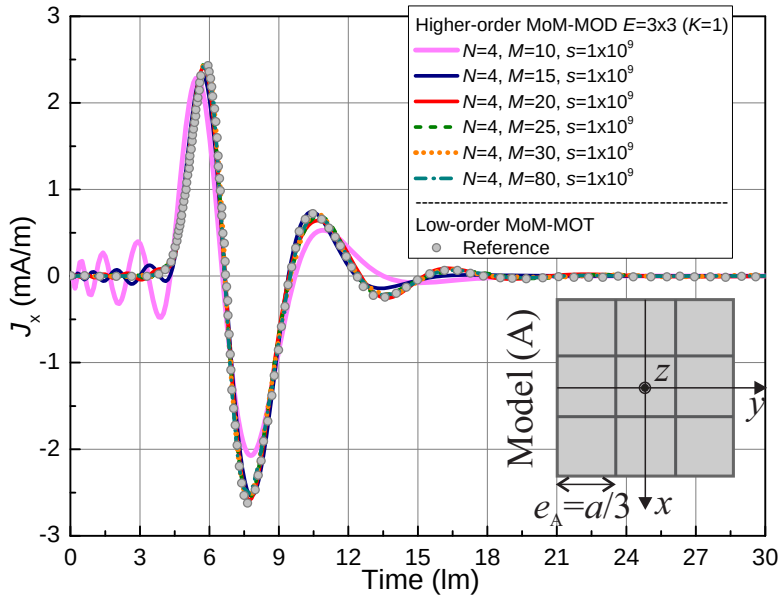

(a)

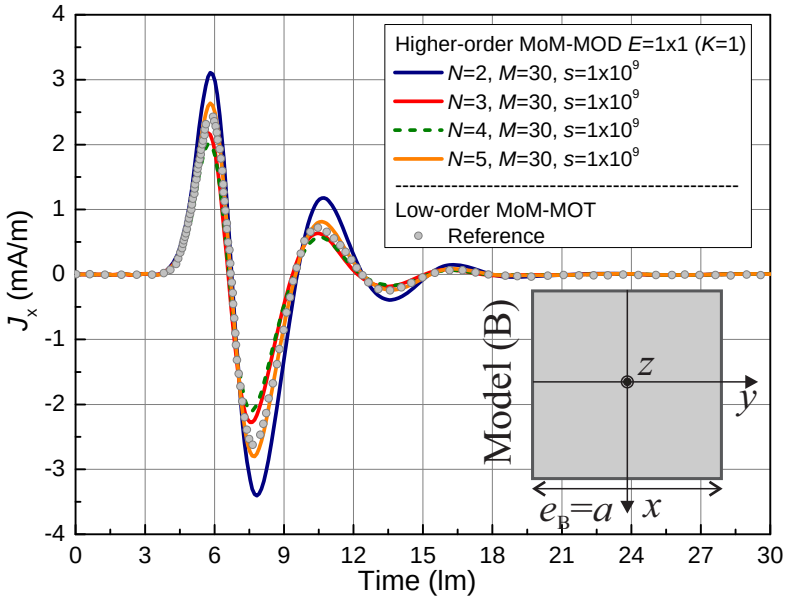

(b)

Figure 4.3. Convergence analysis of the presented MoM-MOD method for a metallic square plate scatterer in terms of the orders of temporal and spatial basis functions, M and $N_u = N_v = N$, in computing transient responses of the x-directed surface current density at the center of the plate: (a) increasing M for a fixed N in model (A) (plate subdivided into 3 × 3 SIE elements) and (b) p-refinement of model (B) (entire-domain model, with a single SIE element) for a fixed M. The higher order results are compared with the low-order MoM-MOT solution [45].

RWG spatial basis functions and triangular temporal basis functions). We observe from the figure that the higher order results converge monotonically and quickly with the *p*-refinement and that the solution corresponding to $N = 5$, resulting in $N_{\text{MoM}} = 40$ unknowns only, agrees very well with the reference solution. With the entire-domain model (B), N_{MoM} is reduced by a factor of 6.6 with respect to model (A) with $N = 4$, and by a factor of 3.8 when compared to the reference solution [45].

4.3 Cubical Scatterer – Structure with Flat Surfaces and Sharp Edges

As the second example of structures with flat surfaces and sharp edges, we consider the transient current response over sides of a PEC cube of edge length $a = 1$ m. For the incident wave in (4.1), $\mathbf{E}_0 = E_0\hat{\mathbf{x}}$, ($E_0 = 1$ V/m) and $\hat{\mathbf{k}} = -\hat{\mathbf{z}}$, which corresponds to the azimuthal angle $\phi = 0^{\text{o}}$ and elevation angle $\theta = 0^{\text{o}}$, as depicted in Fig. 4.1, and the Gaussian pulse is defined for two different cases of the analysis. In case (i), we adopt $T_{\text{w}} = 8$ lm and $t_0 = 12$ lm, so that the pulse frequency spectrum has a practical upper bound of $f_{\text{max1}} = 125$ MHz, and thus its band does not contain internal resonances of the cube, the lowest of which occurs at $f_{\text{res1}} = 212.13$ MHz. For case (ii), $T_{\text{w}} = 2$ lm and $t_0 = 3$ lm, resulting in the upper frequency bound of $f_{\text{max2}} = 500$ MHz for the covered frequency band, which includes the first six resonances of the cube ($f_{\text{res2}} = 259.81$ MHz, $f_{\text{res3}} = 335.41$ MHz, $f_{\text{res4}} = 367.42$ MHz, $f_{\text{res5}} = 424.26$ MHz, $f_{\text{res6}} = 450.00$ MHz). For the temporal approximation in the method, we adopt $M = 130$ and $s = 10^8$ in case (i) and $s = 3\times10^8$ in case (ii). In addition, we consider two different spatial models of the cube: (A) the cube subdivided uniformly with three subdivisions per edge, which results in 54 flat ($K_u = K_v = K = 1$) quadrilateral patches (squares) (note that $e_{\text{A}} = a/3 \approx 0.13\lambda$ at f_{max1}), with $N_u = N_v = N = 2$ and $N_{\text{MoM}} = 432$ and (B) the cube modeled using only six flat surface elements representing the six

cube faces ($e_B = a = 0.42\lambda$ at f_{max1} and $e_B = a = 1.667\lambda$ at f_{max2}), with $N = 5$ and $N_{MoM} = 300$. Figs. 4.4(a) and (b)–(c) show, respectively, the transient current responses in the nonresonant band [excitation case (i)] obtained simulating both models (A) and (B) and the resonant band [excitation case (ii)] using model (B) only. The higher order MoM-MOD results are compared with low-order implicit MoM-MOT TD CFIE solutions (using 832 triangular patches and 1,248 spatial unknowns) reported in [69], and an excellent agreement of the two sets of the results is observed.

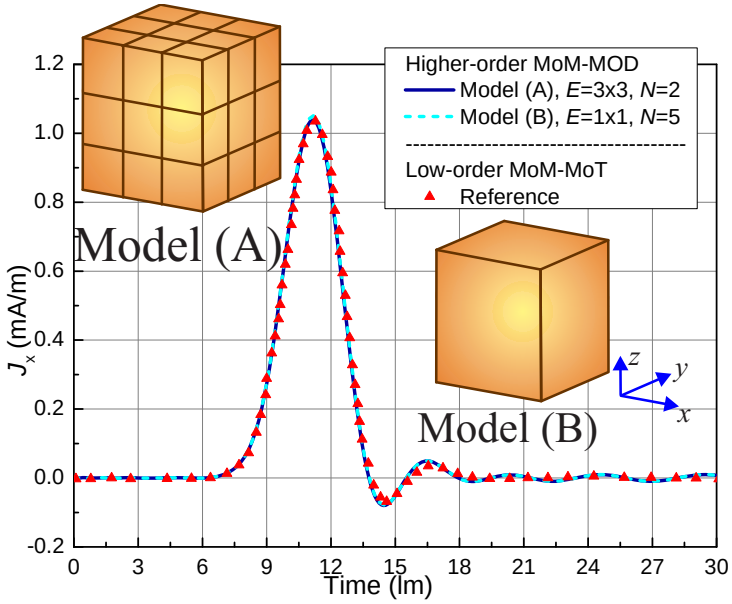

(a)

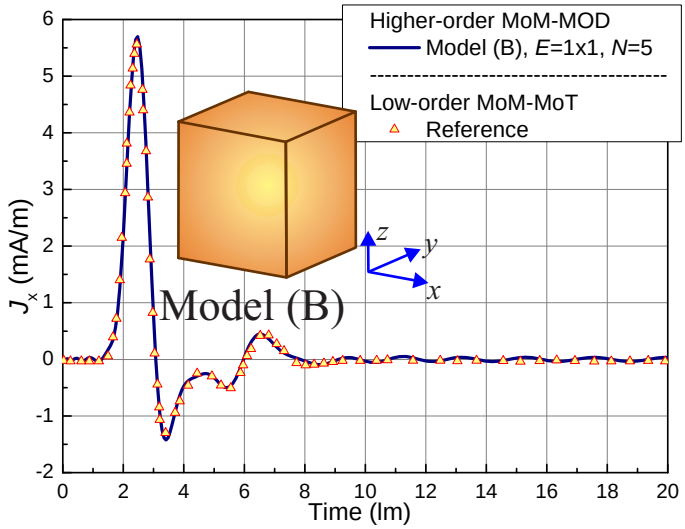

(b)

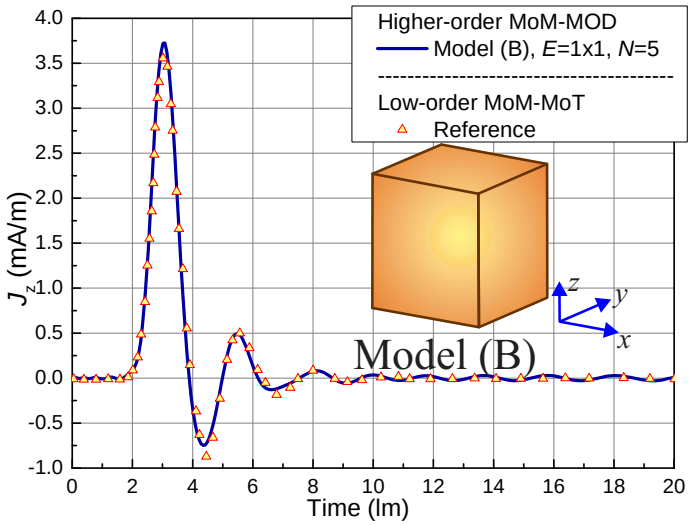

(c)

Figure. 4.4. Comparison of results obtained by the presented MoM-MOD TD EFIE method and low-order implicit MoM-MOT TD CFIE solutions [69] for the transient current response of a PEC cubical scatterer: (a) *x*-directed surface current density at the center of the top face of the cube in the nonresonant band [excitation case (i)] for two different models (A) and (B) shown in the inset; and (b) *x*-directed J_S at the center of the top face and (c) *z*-directed J_S at the center of the side face of the cube in the resonant band [excitation case (ii)] using model (B) only.

4.4 Spherical Scatterer – Structure with Pronounced Curvature

As the first example of structures with pronounced curvature, we next analyze a metallic spherical scatterer, of radius $a = 0.5$ m, illuminated as in Fig. 4.1 with $\mathbf{E}_0 = E_0\hat{\mathbf{x}}$, ($E_0 = 1$ V/m), $\hat{\mathbf{k}} = -\hat{\mathbf{z}}$, finite duration of the signal $T_f = 40$ lm, and cases (i) and (ii) from the previous example (note that the first three internal resonances of the sphere are $f_{res1} = 262.02$ MHz, $f_{res2} = 369.77$ MHz, and $f_{res3} = 429.06$ MHz). Spatial modeling of the sphere is performed using only six equal generalized quadrilateral SIE patches with geometrical orders (A) $K_u = K_v = K = 2$ and (B) $K = 4$, respectively ($e_A = e_B \approx 0.36\lambda$ at f_{max1} and $e_A = e_B \approx 1.34\lambda$ at f_{max2}). Figs. 4.5(a) and (b) show the convergence of the presented MoM-MOD method with respect to polynomial orders of spatial and temporal approximations, respectively, of the *z*-component of $\mathbf{J}_S$ at the center of one of the six patches (this point belongs to the central equator of the sphere) in model

(A) in excitation case (i). Based on these results, the optimal polynomial orders of spatial and temporal basis functions of the Hertz vector (current), in (3.8) and (3.9), are found to be $N_u = N_v = N = 2$, which yields $N_{\text{MoM}} = 48$, and $M = 130$ (with $s = 10^8$), respectively, for this example, and the agreement with results obtained by a low-order MoM-TD EFIE technique (528 flat triangular patches and 792 spatial unknowns) in conjunction with a conventional MOD [52] is observed to be excellent. The convergence of the higher order results in terms of the geometrical order of modeling for excitation case (ii), where $N = 4$ and only 192 unknowns suffice, is presented in Fig. 4.5(c). Both models (A) and (B) provide an excellent accuracy of results when compared to the reference solution [52], but the results obtained with $K = 4$ can be observed to be in a better agreement with the reference solution at the current peak than those with $K = 2$. Note also that the more accurate curved geometrical model with only six higher order SIE elements reduces the number of spatial unknowns by a factor of 16.5 in case (i), and by a factor of 4.1 in case (ii), when compared to the reference model [52].

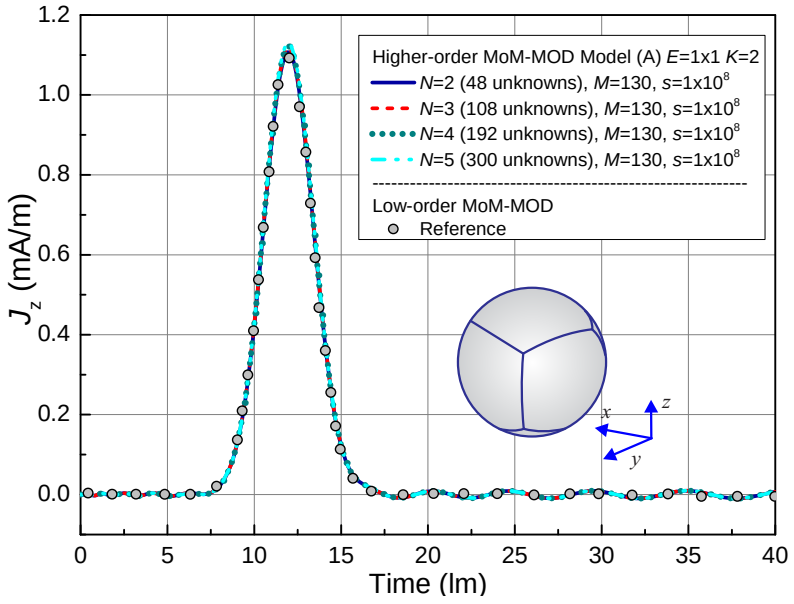

(a)

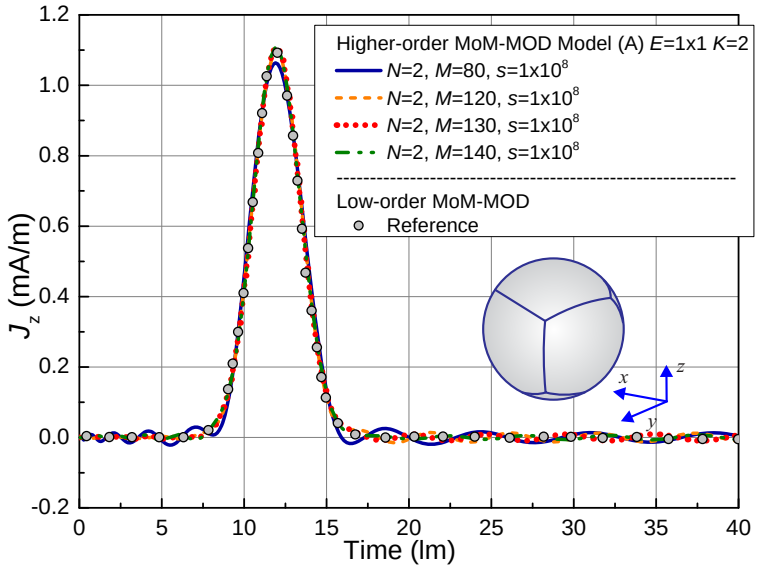

(b)

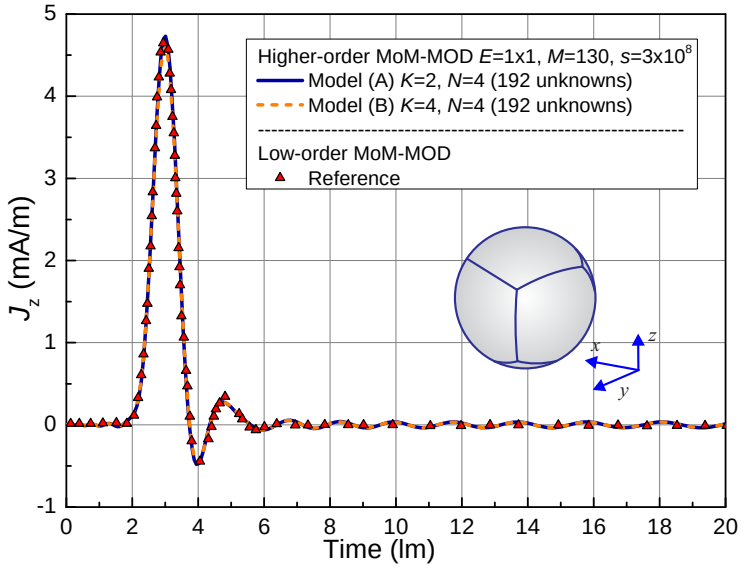

(c)

Figure. 4.5. Convergence of results for a metallic spherical scatterer obtained by the presented MoM-MOD method with respect to polynomial orders of (a) spatial and (b) temporal approximations of the *z*-component of $\mathbf{J}_S$ at the center of one of the six patches in model (A) ($K_u = K_v = K = 2$) shown in the figure inset in the nonresonant band [excitation case (i)], and (c) convergence of the method in terms of the geometrical order K of modeling in the resonant band [excitation case (ii)]. The higher order solutions are compared with results using the low-order MoM-MOD method [52].

To examine the convergence of the presented MoM-MOD with spatial refinement (*h*-refinement), in Fig. 4.6 we plot the relative error of the current, with respect to the analytical

solution obtained by Mie series, for the sphere from Fig. 4.5(c), in the frequency domain. The frequency domain current is obtained from the MoM-MOD solution using DFT and the relative error with respect to Mie series is averaged in the frequency range from 25 MHz to 300 MHz as

$$\text{Error}[\%] = \frac{1}{N_\text{f}} \sum_{i=1}^{N_\text{f}} \left| \frac{\text{J}_i^{\text{SIE}}(\theta,\phi)}{\text{J}_i^{\text{Mie}}(\theta,\phi)} - 1 \right| \cdot 100 \,, \tag{4.2}$$

where $N_\text{f} = 12$ is the number of frequency samples, for fixed $\theta = 90^\text{o}$ and $\phi = 180^\text{o}$ defining the point on the spherical surface in which the currents are computed and compared. The figure shows a family of curves with three representative polynomial current approximations $N = 2$, $N = 3$, and $N = 5$, kept constant for all elements in respective meshes. The points on the $N = 2$ curve correspond, from left to right, to each of the six faces of the sphere from Fig. 4.5(c) being uniformly refined into 2×2, 4×4, and 6×6 elements, respectively.

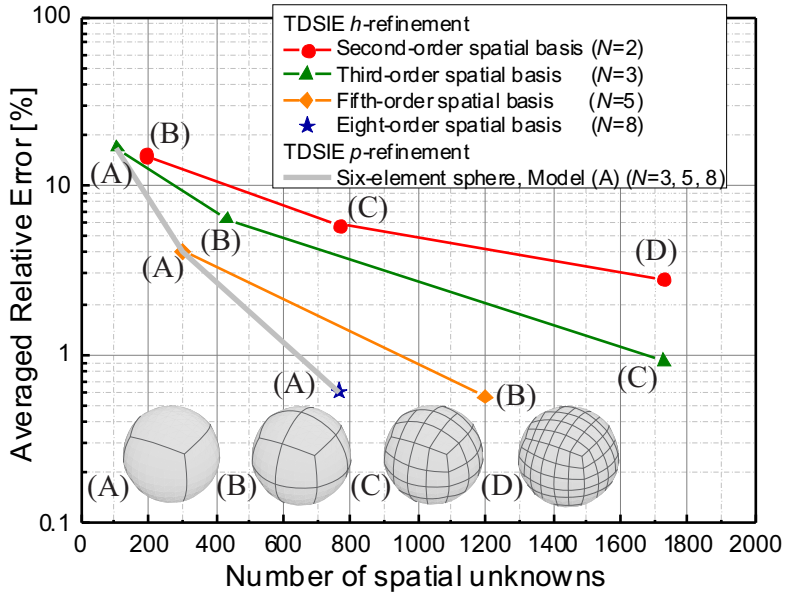

Figure 4.6. Relative error of the TDSIE MoM-MOD computed frequency-domain current averaged in the frequency range from 25 MHz to 300 MHz vs. the number of (spatial) MoM unknowns. A family of three curves obtained using models with three constant polynomial expansion orders N across all the elements shows convergence of the solution with an h-refinement of the mesh, while the fourth curve shows p-refinement of the solution for geometrical model (A).

Similarly, the points on the $N = 3$ curve correspond to a refinement of each of the faces into 1×1, 2×2, and 4×4 elements, and finally the points on the $N = 5$ curve correspond to a refinement of each of the faces into 1×1 and 2×2 elements. All meshes are shown in the figure inset.

We observe from Fig. 4.6 that the method yields monotonic convergence with *h*-refinement and that higher order polynomial current approximation yields better convergence than the lower order expansion. Note also that in this example our lowest achievable error is around 0.55%, which is consistent with the lowest errors achieved by the CFIE based MOT for the PEC sphere example reported in [38]. At the same time, we remark that the error of 0.56%, i.e., close to the minimum error limit, is achieved very quickly with $N = 5$ in our example, hence only two points are shown on this curve. We finally note that our solution with the 0.55% error in computed current yields 0.05% relative error in the computation of the radar cross section (RCS), which is consistent with the lowest reported errors in [37]. In addition, we show in Fig. 4.6 *p*-refinement of the solution for three different spatial current approximation orders $N = 3$, 5, and 8 on the same geometrical model, model (A), with only six large SIE elements of the fourth geometrical order, $K = 4$ (element size is $e \approx 1.34\lambda$ at f_{max2}). Note that model (A) with $N = 8$ reduces the number of spatial unknowns 1.56 times when compared to model (B) with $N = 5$ while maintaining almost the same accuracy, the error being 0.61%. Also, when compared to model (C) with $N = 2$ for the same number of spatial unknowns ($N_{MoM} = 768$), the error is reduced 10 times. Investigating further the convergence of the MoM-MOD with increasing the maximal order of the time domain basis *M*, shown in Fig. 4.7 is the averaged relative error of the frequency-domain current (computed with respect to the analytical Mie series solution in the same way as for the example in Fig. 4.6, using (4.2)). The family of curves in Fig. 4.7 is chosen as follows. Starting from the first curve on the top (curve I), we have a mesh where each of the 6

sphere faces is divided into 3×3 elements, model (E), with the polynomial current approximation order $N = 2$, which yields 54 elements and $N_{\text{MoM}} = 432$ unknowns. This mesh is then *h*-refined, so that the 6 sphere faces are divided into 6×6 elements, model (D) in Fig. 4.6, and the polynomial current approximation order is kept the same ($N = 2$), which results in 216 elements and $N_{\text{MoM}} = 1{,}728$ unknowns, and the error of the model in this arrangement is given via the second curve from the top (curve II). The third curve from the top (curve III) is obtained utilizing a mesh where each of the 6 sphere faces is divided into 2×2 elements, model (B) in Fig. 4.6, with the polynomial current approximation order $N = 4$, which yields 24 elements and $N_{\text{MoM}} = 768$ unknowns. Similarly as before, this mesh is *h*-refined so that the 6 sphere faces are divided into 3×3 elements, model (E) in Fig. 4.7, and the polynomial current approximation order is kept the same ($N = 4$), which gives 54 elements and $N_{\text{MoM}} = 1{,}728$ unknowns, and the error of the model in this arrangement is shown as the bottom curve (curve IV).

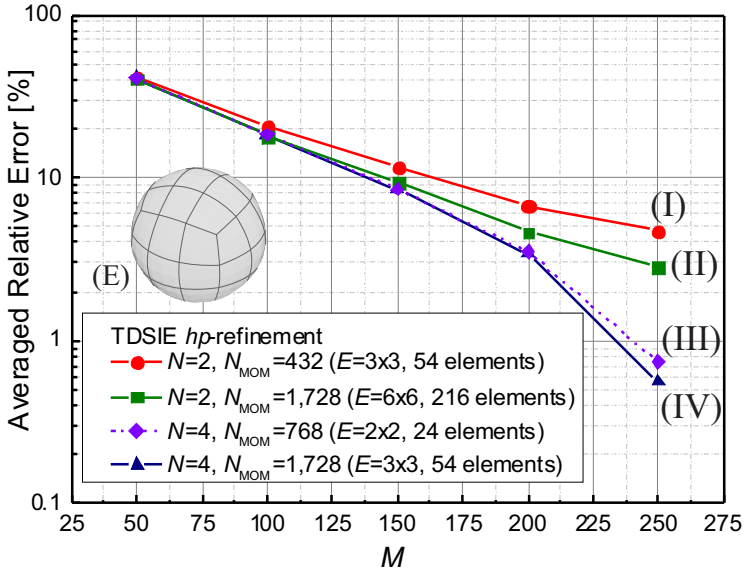

Figure 4.7. Relative error of the TDSIE MoM-MOD computed frequency-domain current averaged in the frequency range from 25 MHz to 300 MHz vs. the order of the time-domain bases *M*. Two sets of curves, with polynomial expansion orders across all the elements in the mesh equal to $N = 2$ and $N = 4$, both shown for models with a coarse and an *h*-refined mesh, demonstrate the convergence of the solution with respect to *p*- and *h*-refinement, as well as with increase of the temporal bases order, *M*.

We conclude from Fig. 4.7 that increasing M, i.e, marching-on-in-degree, yields monotonic convergence in all cases. At the same time, we see that h-refinement (e.g., going from curve I to curve II) yields only slightly lower error (about 2%) while increasing the number of unknowns four times. Similarly, going from curve III to curve IV, the error decreases only slightly while more than doubling (2.25 times) the number of unknowns. (Note that the minimal error is practically reached for $M = 250$ in both curve III and curve IV.) On the other hand, going from curve I to curve III, by increasing N from 2 to 4, i.e., with a p-refinement of the solution, much faster convergence is achieved while the number of unknowns is increased only about 1.78 times.

4.5 NASA Almond – Electromagnetic Code Consortium (EMCC) benchmark target

The next example presents the higher order MoM-MOD transient analysis of a standard benchmarking structure – NASA almond [70] of the maximum length (from the tip to the tail of the almond) $l_{\max} = 1$ m, illuminated as in Fig. 4.1 with $\mathbf{E}_0 = 377\ \text{V/m}\,\hat{\mathbf{x}}$, $\hat{\mathbf{k}} = -\hat{\mathbf{z}}$, $T_f = 30$ lm, $T_w = 4$ lm, $t_0 = 6$ lm, and $f_{\max} = 250$ MHz. The almond is modeled using only 56 quadrilateral surface elements ($e \leq 0.1\lambda$ at $f_{\max}$) of second geometrical order ($K_u = K_v = K = 2$), as portrayed in Fig. 4.8(a), and the other numerical parameters of the model are $N_u = N_v = 2$, $N_{\text{MoM}} = 448$, $M = 130$, and $s = 3\times10^8$. Shown in Fig. 4.8(b) is the transient response of the current density at the center of the top surface of the almond. The results obtained by the presented MoM-MOD are compared with a low-order MoM-MOD solution (864 flat triangular elements, 1,296 spatial unknowns, and $M = 128$) [71], and we observe an excellent agreement of the two sets of MoM-MOD results.

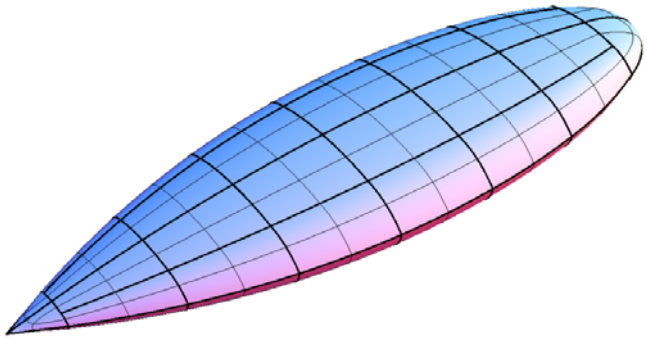

(a)

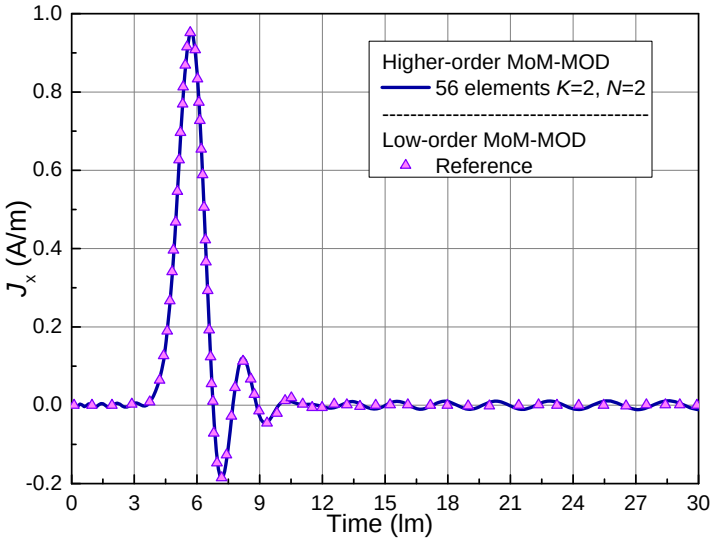

(b)

Figure 4.8. MoM-MOD scattering analysis of the NASA metallic almond: (a) geometrical model with 56 curved quadrilateral SIE patches and (b) comparison of results for the transient response of the *x*-directed surface current density at the center of the top face of the almond obtained by the presented MoM-MOD and the low-order MoM-MOD solution [71].

4.6 Realistic Model of a Military Tank

As the last example, we analyze a more complex structure such as a military tank of dimensions 4 m × 9 m × 2.73 m, shown in Fig. 4.9(a) [note that this tank has approximately the same dimensions as T-80 series tank]. The structure is illuminated with a θ-polarized Gaussian pulse of amplitude E_0 = 1 V/m impinging from the direction defined by $\theta = 90^o$ and $\phi = 0^o$ (Fig. 4.1), with T_w = 70 lm, t_0 = 90 lm, and f_{max} = 15 MHz. The tank is modeled using only 147 surface

elements with $K_u = K_v = K = 1$ [as indicated in Fig. 4.9(a)] and $e_{max} \approx 0.315\lambda$ at f_{max}. The transient response of $\mathbf{J}_S$ at the center of a flat patch on the tank side marked by the red frame in Fig. 4.9(a) is computed using the presented MoM-MOD algorithm with N ranging from 2 to 6, $N_{MoM} = 1{,}389$, $s = 1\times10^8$, and $M = 70$ or 100.

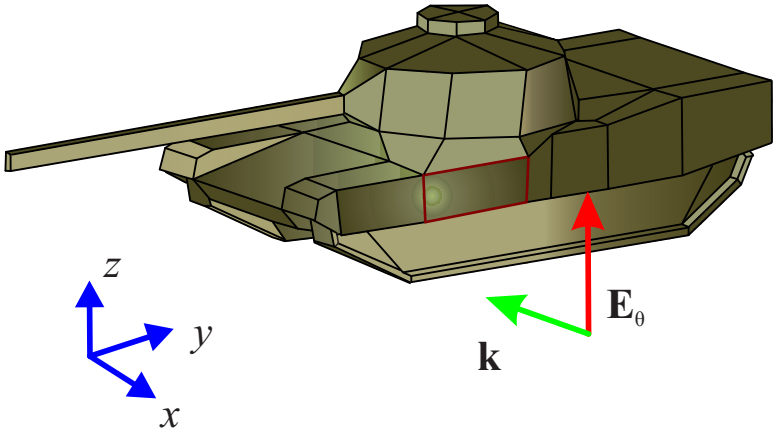

(a)

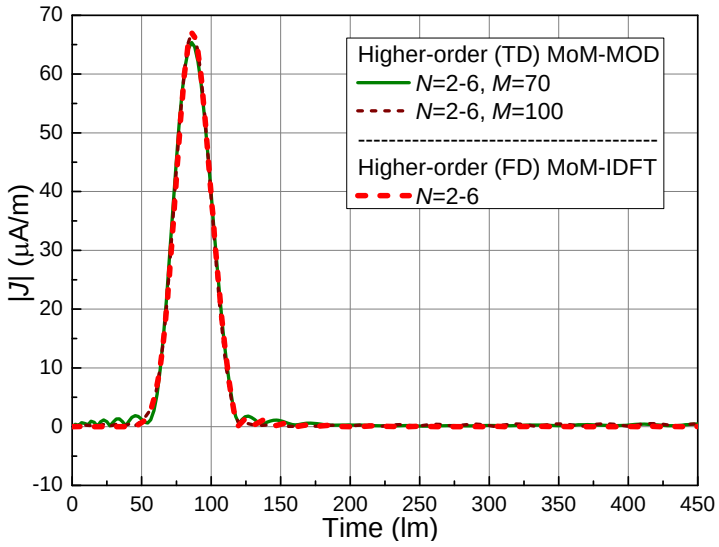

(b)

Figure 4.9. (a) WIPL-D mesh of a military tank consisting of 147 quadrilateral patches with $K_u = K_v = K = 1$ [72] and (b) transient response of $\mathbf{J}_S$ at the center of a flat patch on the tank side marked by the red frame computed using the presented MoM-MOD TD SIE method and the higher order MoM-FD SIE method [60] in conjunction with the inverse discrete Fourier transform.

The solution is compared in Fig. 4.9(b) with frequency-domain results obtained using the higher order MoM-FD SIE method [60] in conjunction with the inverse discrete Fourier transform (IDFT) and computed from DC (extrapolated) to 50 MHz at 128 frequency samples; an excellent agreement of the TD and FD sets of results is observed. For exactly the same spatial model, the computational time for the MoM-FD SIE simulation is 125 min, while the MoM-TD SIE simulation with $M = 70$ takes less than 3 min (computer properties: Intel® Xeon® CPU E5645 @ 2.40 GHz). Note that a similar tank model is analyzed in [58] using low-order small-domain MoM-MOD EFIE and MoM-MOT methods. The model in [58] includes 2,737 triangular flat patches, the spatial distribution of $\mathbf{J}_S$ is expanded in terms of RWG basis functions resulting in 3,905 unknowns, the order of temporal basis functions is $M = 30$, and the excitation is in the form of a triangular pulse with the frequency bandwidth of 50 MHz. The reported simulation times for this model are 1,012 min and 938 min for the MoM-MOD and MoM-MOT methods, respectively. With an assumption that the simulations in [58] are performed on a standard PC with similar or closely comparable hardware (computer used is not specified in [58]), we may conclude that the present method comes out to be much more efficient than methods in [58].

4.7 Conclusion

The method has been validated and evaluated in six characteristic numerical examples, solving for the induced transient surface current densities, as the most rigorous and critical representative of the solution accuracy in MoM-SIE modeling, and assuming that the accuracy of far field computations is even better. The results have demonstrated excellent accuracy, efficiency, convergence, and versatility of the method, which appears to be the first MoM-TD SIE method with very high spatial and temporal expansion orders (the results have demonstrated

using current expansions of spatial orders from 2 to 8 and geometrical-mapping orders from 1 to 4 in conjunction with higher order, entire-domain Laguerre temporal bases) and the first large-domain MoM-MOD method with spatially higher order expansions. They have also demonstrated very effective spatially large-domain MoM-TD SIE models of scatterers using flat and curved patches of electrical sizes of up to about 1.7 wavelengths at the maximum frequency in the frequency spectrum of the pulse excitation and minimal numbers of unknowns, which appear to be the first set of spatially large-domain MoM-TD SIE modeling examples. Moreover, the proposed method shows great potential for *p*- and *hp*-refinement.

5 SUGGESTIONS FOR FUTURE RESEARCH

5.1 Introduction

Transient scattering analysis of 3-D metallic structures using novel higher order TD-MoM EFIE method has been introduced in chapter 3. Hence, this chapter will focus on generalized higher order TD-MoM-MOD method for the scattering analysis of arbitrarily shaped 3-D composite (metallic and dielectric) structures in TD. The geometry of a scatterer is modeled using the same generalized quadrilaterals of arbitrary geometrical orders presented in section 3.3. Formulation of the method is based on two sets of surface integral equations, EFIE and MFIE, discretized and solved by higher order Galerkin-type MoM-MOD approach. In the solution procedure, both integral equations are discretized using spatial higher order divergence-conforming vector polynomial basis functions and orthogonal set of Laguerre polynomials as temporal basis functions (explained in section 3.4). Here, we will outline the main set of equations for generalized higher order MoM-MOD TDSIE.

5.2 Coupled EFIE-MFIE Formulation in TD for Composite Metallic-Dielectric Structures

Consider an EM system consisting of metallic and dielectric bodies excited by Gaussian pulse. According to the surface equivalent principle, we can break the entire system into subsystems, each representing one of the dielectric domains, together with the belonging metallic surfaces, with the remaining space being filled with the same medium. One of the domains is the external space surrounding the structure. The scattered electric and magnetic fields, **E** and **H**, in

each domain can be expressed in terms of equivalent (artificial) surface electric current density $\mathbf{J}_S$, and equivalent (artificial) surface magnetic current density $\mathbf{M}_S$ which are placed on the boundary surface of the domain, with the objective to produce a zero total field in the surrounding space. On the metallic surfaces, only the surface electric currents exist ($\mathbf{J}_S$, these are actual currents) and $\mathbf{M}_S = 0$. The boundary conditions for the tangential components of the total (incident plus scattered) electric and magnetic field vectors on the boundary surface between any two adjacent dielectric domains (domains 1 and 2) yield

$$\begin{aligned}
&[\mathbf{E}(\mathbf{J}_S(\mathbf{r},t),\mathbf{M}_S(\mathbf{r},t),\varepsilon_1,\mu_1)]_{\text{tang}} + (\mathbf{E}_i(\mathbf{r},t))_{\text{tang}} = [\mathbf{E}(-\mathbf{J}_S(\mathbf{r},t),-\mathbf{M}_S(\mathbf{r},t),\varepsilon_2,\mu_2)]_{\text{tang}},\\
&[\mathbf{H}(\mathbf{J}_S(\mathbf{r},t),\mathbf{M}_S(\mathbf{r},t),\varepsilon_1,\mu_1)]_{\text{tang}} + (\mathbf{H}_i(\mathbf{r},t))_{\text{tang}} = [\mathbf{H}(-\mathbf{J}_S(\mathbf{r},t),-\mathbf{M}_S(\mathbf{r},t),\varepsilon_2,\mu_2)]_{\text{tang}},\\
&\mathbf{r}\in S,\quad (\forall)\, t\geq 0
\end{aligned} \tag{5.1}$$

where we assume that the incident field is present only in domain 1. On the conducting (PEC) bodies, the boundary conditions in (5.1) reduce to (3.1), $(\mathbf{E}_{\text{tot}})_{\text{tang}} = 0$. In the presence of electric and magnetic currents, the scattered electric and magnetic fields are expressed in terms of magnetic and electric vector potentials, $\mathbf{A}$ and $\mathbf{F}$, and the electric and magnetic scalar potentials, Φ and U, as

$$\mathbf{E} = -\frac{\partial \mathbf{A}}{\partial t} - \nabla\Phi - \frac{1}{\varepsilon}\nabla\times\mathbf{F}, \qquad \mathbf{H} = -\frac{\partial \mathbf{F}}{\partial t} - \nabla U + \frac{1}{\mu}\nabla\times\mathbf{A}. \tag{5.2}$$

The potentials $\mathbf{A}$ and Φ are computed in (3.3) and (3.4), and analogous expressions hold for the potentials $\mathbf{F}$ and U, in terms of the current density $\mathbf{M}_S$

$$\mathbf{F}(\mathbf{r},t) = \frac{\varepsilon}{4\pi}\int_S \frac{\mathbf{M}_S(\mathbf{r}',t-R/c)}{R}\,\mathrm{d}S \tag{5.3}$$

$$U(\mathbf{r},t) = \frac{1}{4\pi\mu}\int_S \frac{\rho_{mS}(\mathbf{r}',t-R/c)}{R}\,\mathrm{d}S = -\frac{1}{4\pi\mu}\int_S \int_0^{t-R/c} \frac{\nabla_s\cdot\mathbf{M}_S(\mathbf{r}',t')}{R}\,\mathrm{d}t'\mathrm{d}S. \tag{5.4}$$

The magnetic current density vector, $\mathbf{M}_S$, and the magnetic surface charge density, ρ_{mS}, are expressed in terms of the magnetic Hertz vector, $\mathbf{h}^m$, in analogous fashion, see (3.7) and (3.8).

Note that the system of equations (5.1) could be solved for $\mathbf{J}_S$ and $\mathbf{M}_S$ as unknowns directly, but in order to avoid the temporal integration in (3.4) and (5.4), Hertz vectors are introduced as actual unknowns in the MoM solution procedure [65]. Boundary conditions in (5.1) with field and potential expressions (5.2), (3.3), (3.4), (5.3) and (5.4), respectively, represents a set of coupled EFIE and MFIE which are discretized and solved using MoM-MOD with full Galerkin testing as explained in chapter 3, sections 3.5 and 3.6.

5.3 Hybrid Higher Order FEM-MoM Modeling in TD

In order to extend the range of real-world transient EM applications including electrically large homogenous/inhomogeneous problems, one possibility for further research is to hybridize the TD-FEM and the TD-MoM in a higher order TD-FEM-MoM fashion. Similar work in the frequency domain has been reported in [5] for scattering analysis of arbitrary structures. Inhomogeneous objects will be discretized by the higher-order FEM [11], which is a significant advantage as compared to the pure MoM-SIE approach.

Finally, to enhance the efficiency of both the TD-FEM and the TD-MoM, as well as the hybrid TD-FEM-MoM, special parallel versions of the TD higher order methods based on GPU (graphics processing unit) acceleration may be developed as future work.

6 CONCLUSIONS

This dissertation has developed and demonstrated two novel general CEM methods for transient analysis of closed (waveguide and cavity based) and open (radiation and scattering) structures, respectively, employing two different numerical approaches directly in time domain.

The first method is novel higher order and large-domain Galerkin FEM for transient analysis of multiport microwave waveguide devices. It is based on geometrical modeling using Lagrange interpolation generalized hexahedral elements, spatial field expansion in terms of hierarchical curl-conforming polynomial vector basis functions, time-stepping with an implicit unconditionally stable finite difference scheme using the Newmark-beta method, and mesh truncation introducing the waveguide port boundary condition. This method is developed and extensively tested on numerous waveguide sections with sharp edges and pronounced curvatures including metallic and/or dielectric discontinuities. The results obtained by the higher order TDFEM are in an excellent agreement with the higher order FDFEM-DFT/IDFT solutions, as well as with measurements and with alternative full-wave numerical solutions in both time and frequency domains.

The second method is a novel higher order and large-domain Galerkin MoM in conjunction with the SIE formulation for transient analysis of antennas and scatterers of arbitrary shapes and metallic/dielectric material compositions. The method applies higher order conformal Lagrange generalized curved parametric quadrilateral patches and hierarchical divergence-conforming polynomial vector basis functions for spatial current distributions, approximation of time variations by orthogonal temporal basis functions derived from Laguerre polynomials, and iterative solution of the final system of spatially and temporally discretized SIE equations in a

MOD fashion. This method has been implemented for transient scattering analysis of metallic objects. Preliminary results are obtained for electrically large PEC 3-D structures such as cube, sphere, NASA almond, and military tank, by solving EFIE in TD using higher order MoM technique in conjunction with MOD method (MoM-MOD TDEFIE). These results, obtained with less than 1,500 spatial unknowns, are compared with low-order small-domain numerical techniques, and the agreement is very good. In order to perform transient analysis of dielectric and composite (metallic and dielectric) structures this method will be extended to generalized higher order MoM-MOD TDSIE, including both field formulations, EFIE and MFIE.

Finally, higher order TD-FEM and TD-MoM show excellent performance in terms of geometrical modeling accuracy and flexibility as well as higher order modeling of transient field/current propagation through electrically large elements. The ultimate goal of the dissertation is to provide accurate, stable, and efficient transient solution to real-world applications.

7 REFERENCES

[1] J. M. Jin, *The Finite Element Method in Electromagnetics*, 2nd ed., John Wiley & Sons, New York, 2002.

[2] P. P. Silvester and R. L. Ferrari, *Finite Elements for Electrical Engineers*, 3rd ed. Cambridge, U.K.: Cambridge Univ. Press, 1996.

[3] J. L. Volakis, A. Chatterjee, and L. C. Kempel, *Finite Element Method for Electromagnetics*. New York, NY, USA: IEEE Press, 1998.

[4] M. M. Ilić and B. M. Notaroš, "Higher order hierarchical curved hexahedral vector finite elements for electromagnetic modeling," *IEEE Transactions on Microwave Theory and Techniques*, vol. 51, no. 3, pp. 1026–1033, March 2003.

[5] M. M. Ilić, M. Djordjević, A. Ž. Ilić, and B. M. Notaroš, "Higher order hybrid FEM-MoM technique for analysis of antennas and scatterers," *IEEE Transactions on Antennas and Propagation,* vol. 57, no. 5, pp. 1452–1460, May 2009.

[6] J. M. Jin and D. J. Rieley, *Finite element analysis of antennas and arrays*. New York, NY, USA: Wiley, 2009.

[7] J. Rubio, J. Arroyo, and J. Zapata, "Analysis of passive microwave circuits by using a hybrid 2-D and 3-D finite-element mode-matching method," *IEEE Transactions on Microwave Theory and Techniques*, vol. 47, no. 9, pp. 1746–1749, September 1999.

[8] J. Liu, J. M. Jin, E. K. N. Yung, and R. S. Chen, "A fast, higher order three-dimensional finite-element analysis of microwave waveguide devices," *Microwave and Optical Technology Letters,* vol. 32, no. 5, pp. 344–352, March 5, 2002.

[9] E. Martini, G. Pelosi, and S. Selleri, "A hybrid finite-element—modal-expansion method with a new type of curvilinear mapping for the analysis of microwave passive devices," *IEEE Transactions on Microwave Theory and Techniques*, vol. 51, no. 6, pp. 1712–1717, June 2003.

[10] M. M. Ilić, A. Ž. Ilić, and B. M. Notaroš, "Higher order large-domain FEM modeling of 3-D multiport waveguide structures with arbitrary discontinuities," *IEEE Transactions on Microwave Theory and Techniques*, vol. 52, no. 6, pp. 1608–1614, June 2004.

[11] M. M. Ilić, A. Ž. Ilić, and B. M. Notaroš, "Continuously inhomogeneous higher order finite elements for 3-D electromagnetic analysis," *IEEE Transactions on Antennas and Propagations*, vol. 57, no. 9, pp. 2798–2803, September 2009.

[12] A. C. Cangellaris, C. C. Lin, and K. K. Mei, "Point-matched time-domain finite element methods for electromagnetic radiation and scattering," *IEEE Transactions on Antennas and Propagation,* vol. 35, no. 10, pp. 1160–1173, October 1987.

[13] J. F. Lee, "WETD – A finite element time-domain approach for solving Maxwell's equations," *IEEE Microwave and Guided Wave Letters,* vol. 4, no. 1, pp. 11–13, January 1994.

[14] J. F. Lee, R. Lee, and A. C. Cangellaris, "Time-domain finite element methods," *IEEE Transactions an Antennas and Propagation*, vol. 45, no. 3, pp. 430–442, March 1997.

[15] M. R. Zunoubi, K. C. Donepudi, J. M. Jin, and W. C. Chew, "Efficient time-domain and frequency-domain finite-element solution of Maxwell's equations using spectral Lanczos decomposition method," *IEEE Transactions on Microwave Theory and Techniques,* vol. 46, no. 8, pp. 1141–1149, August 1998.

[16] D. Jiao and J. M. Jin, "Time-domain finite-element modeling of dispersive media," *IEEE Microwave and Wireless Components Letters,* vol. 11, no. 5, pp. 220–222, May 2001.

[17] D. Jiao and J. M. Jin, "Time-domain finite-element simulation of cavity-backed microstrip patch antenna," *Microwave and Optical Technology Letters,* vol. 32, no. 4, pp. 251–254, February 20 2002.

[18] D. Jiao, A. A. Ergin, B. Shanker, E. Michielssen, and J. M. Jin, "A fast higher-order time-domain finite element-boundary integral method for 3-D electromagnetic scattering analysis," *IEEE Transactions on Antennas and Propagation,* vol. 50, no. 9, pp. 1192–1202, September 2002.

[19] D. Jiao and J. M. Jin, "Three-dimensional orthogonal vector basis functions for time-domain finite-element solution of vector wave equations," *IEEE Transactions on Antennas and Propagation,* vol. 51, no. 1, pp. 59–66, January 2003.

[20] D. K. Sun, J. F. Lee and Z. Cendes, "Transfinite-element time-domain method," *IEEE Transactions on Microwave Theory and Techniques,* vol. 51, no. 10, pp. 2097–2105, October 2003.

[21] Z. Lou and J. M. Jin, "An accurate waveguide port boundary condition for the time-domain finite-element method," *IEEE Transactions on Microwave Theory and Techniques,* vol. 53, no. 9, pp. 3014–3023, September 2005.

[22] J. M. Jin, Z. Lou, Y. J. Li, N. W. Riely, and D. J. Riely, "Finite element analysis of complex antennas and arrays," Special Issue on Large and Multiscale Computational Electromagnetics, *IEEE Transactions on Antennas and Propagation*, vol. 56, no. 8, pt. I, pp. 2222–2240, August, 2008.

[23] N. Marais and D. B. Davidson, "Numerical evaluation of high-order finite element time domain formulations in electromagnetics," *IEEE Transactions on Antennas and Propagation*, vol. 56, no. 12, pp. 3743–3751, December 2008.

[24] E. M. Klopf, S. B. Manić, M. M. Ilić, and B. M. Notaroš, "Efficient time-domain analysis of waveguide discontinuities using higher order FEM in frequency domain," *Progress In Electromagnetics Research*, vol. 120, pp. 215–234, 2011.

[25] B. M. Notaroš, "Higher order frequency-domain computational electromagnetics," Special Issue on Large and Multiscale Computational Electromagnetics, *IEEE Transactions on Antennas and Propagation*, vol. 56, no. 8, pp. 2251–2276, August 2008.

[26] M. Abramowitz and I. Stegun, *Handbook of mathematical functions*. New York, NY, USA: Dover, 1970.

[27] S. D. Gedney and U. Navsariwala, "An unconditionally stable finite element time-domain solution of the vector wave equation," *IEEE Microwave and Guided Wave Letters,* vol. 5, no. 10, pp. 332–334, October 1995.

[28] A. E. Yilmaz, D. S. Weile, B. Shanker, J. M. Jin and E. Michielssen, "Fast analysis of transient scattering in lossy media," *IEEE Antennas and Wireless Propagation Letters,* vol. 1, no. 1, pp. 14–17, December 2002.

[29] H. P. Tsai, Y. Wang, and T. Itoh, "Efficient analysis of microwave passive structures using 3-D envelope-finite element (EVFE)," *IEEE Transaction on Microwave Theory and Techniques*, vol. 50, no. 12, pp. 2721–2727, December 2002.

[30] R. Bunger and F. Arndt, "Moment-method analysis of arbitrary 3-D metallic *N*-port waveguide structures," *IEEE Transactions on Microwave Theory and Techniques*, vol. 48, no. 4, pp. 531–537, April 2000.

[31] B. Gimeno and M. Guglielmi, "Multimode Equivalent Network Representation for *H*- and *E*-Plane Uniform Bends in Rectangular Waveguide" *IEEE Transactions on Microwave Theory and Techniques,* vol. 44, no. 10, pp. 1679-1687, October 1996.

[32] A. Weisshaar, S. M. Goodnick, and V. K. Tripathi, "A Rigorous and Efficient Method of Moments Solution for Curved Waveguide Bends " *IEEE Transactions on Microwave Theory and Techniques,* vol. 40, no. 12, pp. 2200–2206, December 1992.

[33] C.L. Bennett, Jr., "A technique for computing approximate electromagnetic impulse response of conducting bodies," Ph.D. dissertation, Purdue University, West Lafayette, Ind., 1968.

[34] S. M. Rao, *Time domain electromagnetics*, Academic Press, 1999.

[35] S. M. Rao and D. R. Wilton, "Transient scattering by conducting surfaces of arbitrary shape," *IEEE Transactions on Antennas and Propagation*, vol. 39, no. 1, pp. 56–61, January 1991.

[36] S. M. Rao and T. K. Sarkar, "An alternative version of the time-domain electric field integral equation for arbitrarily shaped conductors," *IEEE Transactions on Antennas and Propagation*, vol. 41, no. 6, pp. 831–834, June 1993.

[37] R. A. Wildman, G. Pisharody, D. S.Weile, S. Balasubramaniam, and E. Michielssen, "An Accurate Scheme for the Solution of the Time-Domain Integral Equations of Electromagnetics Using Higher Order Vector Bases and Bandlimited Extrapolation,"

IEEE Transactions on Antennas and Propagation, vol. 52. no. 11, pp. 2793–2984, November 2004.

[38] Y. Beghein, K. Cools, H. Bagci, and D. De Zutter, "A Space-Time Mixed Galerkin Marching-on-in-Time Scheme for the Time-Domain Combined Field Integral Equation," *IEEE Transactions on Antennas and Propagation*, vol. 61, no. 3, pp. 1228-1238, March 2013.

[39] Pray, A. J.; Beghein, Y.; Nair, N. V.; Cools, K.; Bagci, H.; Shanker, B., "A Stable Higher Order Space-Time Galerkin Scheme for Time Domain Integral Equations," ArXiv e-prints, arXiv:1401.2435, available on http://arxiv.org/abs/1401.2435

[40] S. M. Rao and T. K. Sarkar, "An efficient method to evaluate the time-domain scattering from arbitrarily shaped conducting bodies," *Microwave and Optical Technology Letters*, vol. 17, no. 5, pp. 321–325, April 1998.

[41] T. K. Sarkar, W. Lee, and S. M. Rao, "Analysis of transient scattering from composite arbitrarily shaped complex structures," *IEEE Transactions on Antennas and Propagation*, vol. 48, no. 10, pp. 1625–1634, October 2000.

[42] B. H. Jung and T. K. Sarkar, "An accurate and stable implicit solution for transient scattering and radiation from wire structures," *Microwave and Optical Technology Letters*, vol. 34, no. 5, pp. 354–359, September 2002.

[43] B. Shanker, A. A. Ergin, K. Aygun, and E. Michielssen, "Analysis of transient electromagnetic scattering from closed surfaces using a combined field integral equation," *IEEE Transactions on Antennas and Propagation*, vol. 48, no. 7, pp. 1064–1074, July 2000.

[44] B. Shanker, A. A. Ergin, M. Lu, E. Michielssen, "Fast analysis of transient electromagnetic scattering phenomena using the multilevel plane wave time domain algorithm," *IEEE Transactions on Antennas and Propagation*, vol. 51, no. 3, pp. 628–641, March 2003.

[45] G. Manara, A. Monorchio, and R. Reggiannini, "A space-time discretization criterion for a stable time-marching solution of the electric field integral equation," *IEEE Transactions on Antennas and Propagation*, vol. 45, no. 3, pp. 527–532, March 1997.

[46] B. Shanker, M. Lu, J. Yuan, and E. Michielssen, "Time domain integral equation analysis of scattering from composite bodies via exact evaluation of radiation fields," *IEEE Transactions on Antennas and Propagation*, vol. 57, no. 5, pp. 1506–1520, May 2009.

[47] Y. Shi, M. Y. Xia, R. S. Chen, E. Michielssen, and M. Lu, "Stable electric field TDIE solver via quasi-exact evaluation of MOT matrix elements," *IEEE Transactions on Antennas and Propagation*, vol. 59, no. 2, pp. 574–585, February 2011.

[48] A. E. Yilmaz, J. M. Jin, and E. Michielssen, "Time domain adaptive integral method for surface integral equations," *IEEE Transactions on Antennas and Propagation*, vol. 52, no. 10, pp. 2692– 2708, October 2004.

[49] H. Bağci, F. P. Andriulli, F. Vipiana, G. Vecchi, and E. Michielssen, "A well-conditioned integral-equation formulation for efficient transient analysis of electrically small microelectronic devices," *IEEE Transactions on Advance Packing*, vol. 33, no. 2, pp. 468–480, May 2010.

[50] T. K. Sarkar and J. Koh, "Generation of a wide-band electromagnetic response through a Laguerre expansion using early-time and low-frequency data," *IEEE Transactions on Antennas and Propagation*, vol. 50, no. 5, pp. 1408–1416, May 2002.

[51] Y. S. Chung, T. K. Sarkar, and B. H. Jung, "Solution of a time-domain magnetic-field integral equation for arbitrarily closed conducting bodies using an unconditionally stable methodology," *Microwave and Optical Technology Letters*, vol. 35, no. 6, pp. 493–499, December 2002.

[52] B. H. Jung, Y. S. Chung, and T. K. Sarkar, "Time-domain EFIE, MFIE, and CFIE formulations using Laguerre polynomials as temporal basis functions for the analysis of transient scattering from arbitrarily shaped conducting structures," *Progress in Electromagnetic Research*, vol. 39, pp. 1–45, 2003.

[53] Y. S. Chung, T. K. Sarkar, B. H. Jung, M. Salazar-Palma, Z. Ji, S. Jang, and K. Kim, "Solution of time domain electric field integral equation using the Laguerre polynomials," *IEEE Transactions on Antennas and Propagation*, vol. 52, no. 9, pp. 2319–2328, September 2004.

[54] B. H. Jung, T. K. Sarkar Y. S. Chung, M. Salazar-Palma, Z. Ji, S. Jang, and K. Kim, "Transient electromagnetic scattering from dielectric objects using the electric field

integral equation with Laguerre polynomials as temporal basis functions," *IEEE Transactions on Antennas and Propagation*, vol. 52, no. 9, pp. 2329–2340, September 2004.

[55] Z. Ji, T. K. Sarkar, B. H. Jung, Y. S. Chung, M. Salazar-Palma, and M. Yuan, "A stable solution of time domain electric field integral equation for thin-wire antennas using the Laguerre polynomials," *IEEE Transactions on Antennas and Propagation*, vol. 52, no. 10, pp. 2641–2649, October 2004.

[56] B. H. Jung, T. K. Sarkar, S. W. Ting, Y. Zhang, Z. Mei, Z. Ji, M. Yuan, A. De, M. Salazar-Palma, and S. M. Rao, "Time and frequency domain solution of EM problems using integral equations and a hybrid methodology," Hoboken, New Jersey: *IEEE Press, John Wiley & Sons, Inc.*, 2010.

[57] Z. Ji, T. K. Sarkar, B. H. Jung, M. Yuan, and M. Salazar-Palma, "Solving time domain electric field integral equation without time variable," *IEEE Transactions on Antennas and Propagation*, vol. 54, no. 1, pp. 258–262, January 2006.

[58] Z. Mei, Y. Zhang, T. K. Sarkar, B. H. Jung, A. García-Lampérez, M. Salazar-Palma, "An improved marching-on-in-degree method using a new temporal basis," *IEEE Transactions on Antennas and Propagation*, vol. 59, no. 12, pp. 4643–4650, December 2011.

[59] S. M. Rao, D. R. Wilton, and A. W. Glisson, "Electromagnetic scattering by surfaces of arbitrary shape", *IEEE Transactions on Antennas and Propagation*, vol. AP-30, pp. 409–418, May 1982.

[60] M. Đorđević and B. M. Notaroš, "Double higher order method of moments for surface integral equation modeling of metallic and dielectric antennas and scatterers," *IEEE Transactions on Antennas and Propagation*, vol. 52, no. 8, pp. 2118–2129, August 2004.

[61] M. J. Bluck and S. P. Walker, "Time-domain BIE analysis of large three-dimensional electromagnetic scattering problems," *IEEE Transactions on Antennas and Propagation*, vol. 45, no. 5, pp. 894–901, May 1997.

[62] M. D. Pocock, M. J. Bluck, and S. P. Walker, "Electromagnetic scattering from 3-D curved dielectric bodies using time-domain integral equations," *IEEE Transactions on Antennas and Propagation*, vol. 46, no. 8, pp. 1212–1219, August 1998.

[63] F. Valdés, M. Ghaffari-Miab, F. P. Andriulli, K. Cools, and E. Michielssen, "High-order Calderón preconditioned time domain integral equation solvers," *IEEE Transactions on Antennas and Propagation*, vol. 61, no. 5, pp. 2570–2588, May 2013.

[64] N. J. Šekeljić, M. M. Ilić and B. M. Notaroš, "Higher order time-domain finite element method for microwave device modeling with generalized hexahedral elements," *IEEE Transactions on Microwave Theory and Techniques*, vol. 61, no. 4, pp. 1425–1434, April 2013.

[65] J. A. Stratton, *Electromagnetic theory*, New York: McGraw-Hill, 1941.

[66] B. D. Popovic and B. M. Notaros, "Moment-method analysis of volume dielectric scatterers. Four independent entire-domain solutions: Is entire-domain philosophy a luxury or necessity in the method of moments?" (invited review paper), *International Journal of Microwave and Millimeter-Wave Computer-Aided Engineering*, vol. 6, (6), pp.454-473, November 1996.

[67] A. D. Poularikas, *The transforms and applications handbook*, Pistcataway, NJ: IEEE Press, 1963.

[68] E. M. Klopf, N. J. Šekeljić, M. M. Ilić and B. M. Notaroš, "Optimal modeling parameters for higher order MoM-SIE and FEM-MoM electromagnetic simulations," *IEEE Transactions on Antennas and Propagation*, vol. 60, no. 6, pp. 2790–2801, June 2012.

[69] B. H. Jung and T. K. Sarkar, "Time-domain CFIE for the analysis of transient scattering from arbitrarily shaped 3D conducting objects," *Microwave and Optical Technology Letters*, vol. 34, no. 4, pp. 289–296, August 2002.

[70] A. C. Woo, H. T. G. Wang, M. J. Schuh, and M. L. Sanders, "Benchmark radar targets for the validation of computational electromagnetics programs," *IEEE Antennas and Propagation Mag.*, vol. 35, no. 1, pp. 84–89, February 1993.

[71] A. Geranmayeh, "Time Domain Boundary Integral Equations Analysis", Ph.D. Dissertation, Vom Fachbereich Elektrotechnik und Informationstechnik der Technischen Universitat Darmstadt, Germany 2011.

[72] WIPL-D d.o.o. 2013. WIPL-D Pro v11.0. Available: http://www.wipl-d.com

8 PUBLICATIONS OF THE CANDIDATE

1. N. J. Šekeljić, M. M. Ilić, and B. M. Notaroš, "Spatially Large-Domain and Temporally Entire-Domain Electric-Field Integral Equation Method of Moments for 3-D Scattering Analysis in Time Domain," accepted, in print to appear in Vol. 63 No. 6 of *IEEE Transactions on Antennas and Propagation*.

2. E. Chobanyan, N. J. Sekeljic, A. B. Manic, M. M. Ilic, V. N. Bringi, and B. M. Notaros, "Efficient and Accurate Computational Electromagnetics Approach to Precipitation Particle Scattering Analysis Based on Higher Order Method of Moments Integral Equation Modeling," *Journal of Atmospheric and Oceanic Technology*, under review.

3. M. Thurai, V. N. Bringi, A. B. Manic, N. J. Sekeljic, and B. M. Notaros, "Investigating rain drop shapes, oscillation modes, and implications for radiowave propagation," *Radio Science*, Vol. 49, Issue 10, October 2014, pp. 921-932.

4. N. J. Šekeljić, M. M. Ilić, and B. M. Notaroš, "Higher Order Time-Domain Finite Element Method for Microwave Device Modeling with Generalized Hexahedral Elements," *IEEE Transactions on Microwave Theory and Techniques*, Vol. 61, No. 4, pp. 1425-1434, April 2013.

5. E. M. Klopf, N. J. Šekeljić, M. M. Ilić, and B. M. Notaroš, "Optimal Modeling Parameters for Higher Order MoM-SIE and FEM-MoM Electromagnetic Simulations", *IEEE Transactions on Antennas and Propagation*, Vol.60, No.6, pp.2790-2801, June 2012.

6. M. M. Ilic, I. Perovic, P. Athalye, N. Sekeljic, A. A. Tonyushkin, B. M. Notaros, "Full-Wave Frequency-Domain Electromagnetic Modelling of RF Fields in MRI Applications," *Proceedings of 2015 IEEE AP-S/URSI International Symposium*, accepted.

7. M. M. Ilic, N. Sekeljic, P. Athalye, A. A. Tonyushkin, B. M. Notaros, "RF Excitation in 7 Tesla MRI Systems Using Monofilar Axial-Mode Helical Antenna," *Proceedings of 2015 IEEE AP-S/URSI International Symposium*, accepted.

8. P. Athalye, N. Sekeljic, M. M. Ilic, A. A. Tonyushkin, B. M. Notaros, "Improving Traveling-Wave RF Fields inside Magnetic Resonance Imaging Bores by Incorporating

Dielectric Loadings," *Proceedings of 2015 IEEE AP-S/URSI International Symposium*, accepted.

9. Branislav M. Notaros, Milan M. Ilic, Alexey A. Tonyushkin, Nada J. Sekeljic, and Pranav Athalye, "Quadrifilar Helical Antenna as a Whole-Body Traveling-Wave RF Coil for 3T and 7T MRI", *Proceedings of 23th International Society for Magnetic Resonance Imaging (ISMRM) 2015*, accepted.

10. N. J. Sekeljic, A. B. Manic, E. Chobanyan, M. Thurai, V. N. Bringi, and B. M. Notaros, "Electromagnetic scattering by oscillating rain drops of asymmetric shapes," *Proceedings of 2014 IEEE Antennas and Propagation Society International Symposium*, July 6-12, 2014, Memphis, Tennessee, pp. 1572-1573.

11. N. J. Sekeljic, S. B. Manic, M. M. Ilic, and B. M. Notaros, "Efficient Models for Transient Analysis of Passive Microwave Devices Using FEM-TD with Time-Marching and FEM-FD with Discrete Fourier Transform," invited paper, Special Session "Time-Domain FEM," *12th International Workshop on Finite Elements for Microwave Engineering – FEM2014*, May 14-17, 2014, Chengdu, China.

12. N. J. Sekeljic, M. M. Ilic, and B. M. Notaros, "p-Refined Large-Domain 3-D Curvilinear FEM Solutions of Arbitrarily Loaded and Shaped Waveguide Sections and Bends in the Time Domain," *Proc. 2014 USNC-URSI National Radio Science Meeting*, January 8-11, 2014, Boulder, Colorado.

13. N. J. Sekeljic, A. Manic, M. M. Ilic, and B. M. Notaros, "Transient Analysis of 3D Waveguides Using Double- Higher-Order Time-Domain Finite Element Method," *Proceedings of 2013 IEEE Antennas and Propagation Society International Symposium*, July 7-12, 2013, Orlando, Florida.

14. E. Chobanyan, N. J. Sekeljic, A. B. Manic, M. M. Ilic, and B. M. Notaros, "Atmospheric Particle Scattering Computation Using Higher Order MoM-SIE Method," *Proceedings of 2013 IEEE Antennas and Propagation Society International Symposium*, July 7-12, 2013, Orlando, Florida.

15. N. J. Sekeljic, S. B. Manic, M. M. Ilic, and B. M. Notaros, "Direct and Indirect Time-Domain FEM Higher Order Solutions to 3-D Closed-Region Problems," *Proc. 2013 USNC-URSI National Radio Science Meeting*, January 9-12, 2013, Boulder, Colorado.

16. N. J. Sekeljic, S. V. Savic, M. M. Ilic, and B. M. Notaros, "Rules for Adoption of Expansion and Integration Orders in FEM Analysis Using Higher Order Hierarchical Bases on Generalized Hexahedral Elements," invited paper, Special Session "Adaptive FEM, Higher Order Bases, and Advanced FEM Formulations," *11th International Workshop on Finite Elements for Microwave Engineering – FEM2012*, June 4-6, 2012, Estes Park, Colorado.

17. B. M. Notaros, M. M. Ilic, S. V. Savic, N. J. Sekeljic, and A. Z. Ilic, "Accurate and Efficient Curvilinear Geometrical Modeling Using Interpolation Parametric Elements in Higher Order CEM Techniques," invited paper, Special Session "Higher Order Numerical Methods", *Proceedings of the 28th International Review of Progress in Applied Computational Electromagnetics – ACES 2012*, April 10-14, 2012, Columbus, Ohio, pp. 602-607.

18. N. J. Sekeljic, E. Chobanyan, M. M. Ilic, and B. M. Notaros, "Rules for Adoption of Expansion and Integration Orders in Moment-Method Computation of Electromagnetic Scattering and Radiation," *Proc. 2012 USNC-URSI National Radio Science Meeting*, January 4-7, 2012, Boulder, Colorado.

19. E. M. Klopf, N. J. Sekeljic, M. M. Ilic, and B. M. Notaros, "Investigations of Optimal Geometrical and Field/Current Modeling Parameters for Higher Order FEM, MoM, and Hybrid CEM Techniques," *Proc. 2011 USNC-URSI National Radio Science Meeting*, January 5-8, 2011, Boulder, Colorado.